Electronic Transport Properties of $LaAlO_3/SrTiO_3$ Heterostructures Under Hydrostatic Pressure

Zur Erlangung des akademischen Grades eines

DOKTORS DER NATURWISSENSCHAFTEN

von der Fakultät für Physik des

Karlsruher Instituts für Technologie (KIT)

Genehmigte Dissertation

von

MSc.Phys. Ahmed Sleem

Tag der mündlichen Prüfung: 10.11.2017

Referent: Prof. Dr. Hilbert von Löhneysen

Korreferent: Prof. Dr. Matthieu Le Tacon

Motivation

The effect of stress on materials has been known for a very long time. It was learned that applying stress on crystalline materials directly changes the distance between atoms which could lead to changes in crystal symmetry. Such modifications consequently alter the physical properties of the material. The effect of stress on physical properties of solids was most widely studied and applied in semiconductor physics, where in 1950 the deformation potential theory was developed by Shockley and Bardeen, relating strain to the conduction band energy shift [1]. Among the simplest applications of stress are epitaxial strain and hydrostatic pressure. The former is generated by depositing thin films of materials on a substrate with slightly different lattice parameters while hydrostatic pressure is achieved by subjecting a sample to equal pressure from all directions.

Epitaxial strain has been used to tune and to induce new properties in semiconducting thin films. For example, it has been used to enhance the electron mobility in silicon based devices, leading to an increase in their switching speed [2]. In strongly correlated transition-metal-oxides, the influence of stress on the electronic properties is expected to be much more pronounced due to the strong coupling of the conduction electrons to the crystal lattice. Even slight distortions of the unit cell may substantially influence crystal fields, orbital occupancy, polarization, and exchange coupling in these oxides [3]. For example, epitaxial strain was used to tune the magnetic properties in $LaCoO_3$ films [4]. Furthermore, $SrTiO_3$(STO) films have been driven ferroelectric with a T_c of 293K [5].

Uniaxial and biaxial strain dominantly affects the symmetry of the unit cell, while keeping the unit-cell volume almost constant, which hinders one from investigating the changes of the electronic properties that are induced by volume changes of the unit cell. However, these changes are accessible and have been explored by applying hydrostatic pressure. For example, it has been used to induce superconductivity in hydrogen sulfide compounds, with transition temperature about 200 K [6]. Also, in high temperature superconducting cuprates, T_c of 164K

was achieved by hydrostatic pressure of 15 GPa [7]. And more recently, hydrostatic pressure of 23 GPa was used to reduce the Curie temperature of $SrRuO_3$ films from 150 to 77 K [8].

The two dimensional (2D) correlated electron system forming at the interface between $LaAlO_3$ (LAO) and $SrTiO_3$ (STO) exhibits symmetry induced splitting of the Ti-3d orbitals. That orbital splitting may be likely influenced by the interatomic distance of the atoms in STO substrate, which greatly influences the electronic properties of the system. In addition to that, the relative permittivity of STO is very sensitive to hydrostatic pressure, especially in the low temperature regime [9]. Hence, the electronic properties of LAO/STO heterostructures are expected to be very sensitive to hydrostatic pressure, motivating measurements of electronic transport under non-ambient conditions, i.e. high pressure and low temperature.

Contents

List of Figures

List of Tables

Chapter 1

Introduction

Artificial heterostructures (AHS's) and superlattices (SL's) have been at the core of condensed matter physics research and device technology over the past decades. Semiconductor HS's and SL's formed the basis for many advances in science and electronic devices. An example is the formation of a 2-dimensional electron gas in III-V-compound semiconductor heterostructures and in metal-oxide-semiconductor field-effect transistors(MOSFET's), which not only led to a breakthrough in device technology, but also represented the basis for the discovery of the quantum Hall effect by von Klitzing et al. [16]. Another example is the giant magneto-resistance in metallic SL's composed of paramagnetic and ferromagnetic layers [17], which are now used as sensing elements in the reading heads of hard disk drives.

At the beginning of this century, numerous efforts have been made to engineer such HS's and SL's using transition metal oxide (TMO) compounds. TMO's can be found in almost every possible electronic ground state such as metallic, insulating, superconducting, ferromagnetic, ferroelectric and more. Many of these compounds show complex phase diagrams with competing ground states due to the delicate interplay of spin-, charge-, orbital and lattice interactions of electrons. External perturbations such as strain, hydrostatic pressure, electric and magnetic fields can very effectively change the orbital ordering patterns of electrons in the 3d bands.

The technological advancements in thin film deposition methods for complex oxides such as Pulsed Laser Deposition (PLD) and Oxide Molecular Beam Epitaxy (MBE), together with the good chemical treatment of substrate and nearly perfect lattice match between many TMO's, made the fabrication of such HS's or SL's a reality. It is expected that combining such TMO's in HS's or SL's would give rise to novel quantum phenomena at their interfaces with properties and functionalities that are not observed in metals or semiconductors.

A prominent example of such heterostructures is the discovery of a highly mobile two dimensional electron system (2DES) at the interface between the two band insulators $LaAlO_3$ (LAO) and $SrTiO_3$ (STO) by Ohtomo and Hwang in 2004 [18]. To explain this discovery, they proposed the polar catastrophe hypothesis, which attributes the formation of the 2DES to the polar discontinuity found at the interface. LAO film layers, i.e. $Al^{3+}O_2^{4-}$ and $La^{3+}O^{2-}$, are charged -1 and +1 respectively, while STO alternates neutral $Ti^{4+}O_2^{4-}$ and $Sr^{2+}O^{2-}$ layers. This polar discontinuity leads to an electric field within the LAO film and an electrostatic potential builds up with increasing LAO film thickness, diverging eventually to infinity. To avoid this catastrophe, the system undergoes electronic reconstruction, resulting in a half elementary charge per formula unit to be transferred from LAO surface to the interface, specifically, to the Ti 3d bands in the top layer of STO substrate. First principles density-functional-theory(DFT) [11] calculations show that in Ti-3d t_{2g} bands, the d_{xy} orbitals, which are degenerate with d_{xz} and d_{yz} in bulk STO, exhibit a drop in their energy of about 250 meV due to the constrained movement of electrons in the direction perpendicular to the sample surface. This drop in the energy of d_{xy} orbitals causes them to become the first orbitals for electrons to occupy, leading to one-type-carrier-transport as long as they are the only occupied orbitals. X-ray spectroscopy has also confirmed the splitting of the usually degenerate Ti-3d t_{2g} bands [19]. This electronic reconstruction not only helps mitigate the effect of the polar catastrophe, but also leads to a metallic interface with a theoretical sheet carrier density of $3.3\text{x}10^{14}$ cm^{-2}, which is the value suggested by the polar catastrophe hypothesis, where half electron per unit cell resides at the interface. However, the sheet carrier density (n_s) reported by other groups lies well below this value [20, 21, 22]. As sheet carrier density increases, a Lifshitz transition takes place between d_{xy} orbitals and the two-fold degenerate d_{xz} and d_{yz} orbitals at $n_c \approx 1.7\text{x}10^{13}$ cm^{-2} [15] leading to two-type-carrier-transport for $n_s > n_c$.

Another possible explanation for the metallic conductivity at the LAO/STO interface is the free electrons left by oxygen vacancies created in the STO substrate during sample growth [23]. The root of this hypothesis comes from the observation that conductive LAO/STO samples are usually grown at low oxygen partial pressure($p(O_2) < 10^{-3}$mbar), while samples grown at high oxygen partial pressure ($p(O_2) > 10^{-2}$mbar)are usually insulating. Ionic intermixing has also been discussed as a source of electrons as well [24]. It is possible for the La^{3+} ions to substitute the Sr^{2+} ions in STO substrate leading to an electron-doping effect. However, it is doubtful that the extent of the intermixing in the system is high enough to generate such high sheet carrier density.

In addition to the metallic conductivity, the interface exhibits a two dimensional superconducting transition, with critical temperature(T_C) of about 250mK [25]. This superconducting transition is found to be sensitive to the charge carrier density at the interface, which can be tuned by applying a back gate voltage to the sample [14]. This tuning allows increase and decrease of n_s by applying positive and negative gate voltage and hence the mapping of the so called "superconducting dome", i.e. T_C versus n_s. The maximum T_C achieved with gate-voltage amounts to about 310 mK.

In this thesis, I will present investigations of the electronic transport properties of LAO/STO heterostructures under hydrostatic pressure. The structure of this work is organised as follows:

In chapter 2 an overview over the basic properties of the constituent materials (LAO and STO) as well as a summary of some important experiments performed on LAO/STO heterostructures under ambient pressure are given. In addition, the different hypotheses that attempt to explain the metallic conductivity at the interface are discussed.

The first part of chapter 3 deals with sample preparation processes, including substrate treatment, thin film growth using PLD as well as the optimization of the growth parameters. After that, the structural properties of the film and the sheet resistance dependence on film thickness are discussed. The final part describes the experimental apparatus and techniques used in order to perform transport measurements under hydrostatic pressure. In chapter 4, the effect of oxygen partial pressure used during growth on the electronic-transport properties of LAO/STO heterostructures at ambient pressure is presented and discussed.

The main part of this work is presented in chapter 5 where the electronic transport properties of LAO/STO heterostructures are investigated under different hydrostatic pressure, ranging from ambient to 1.64 GPa. First, the sheet resistance dependence on hydrostatic pressure is presented and discussed. The second part includes the effect of hydrostatic pressure on the sheet carrier density and Hall mobility. The third part of chapter 5 reports on the magneto transport properties, where magnetoresistance measurements are performed at different temperatures and hydrostatic pressures. The fourth and final part of this chapter deals with the role of electron-electron interaction and weak-localization at temperatures below 10 K. Chapter 6 gives a summary of the work and the results.

Chapter 2

Physical Properties of $LaAlO_3/SrTiO_3$ heterostructures under ambient conditions

2.1 Structural and dielectric properties of the constituents LAO and STO

2.1.1 Structural properties

LAO and STO are non-magnetic band insulators, with band gaps of 5.6 eV and 3.2 eV respectively [26, 27]. Both have crystal structure that belongs to the perovskite family (see Fig.2.1), with a pseudo cubic lattice constant of 3.905 Å for STO [28], and 3.79 Å for LAO [29]. At room temperature and ambient conditions STO displays a cubic structure with Pm3m (221) space group symmetry, whereas LAO shows rhombohedric structure with R-3ch (167) symmetry.

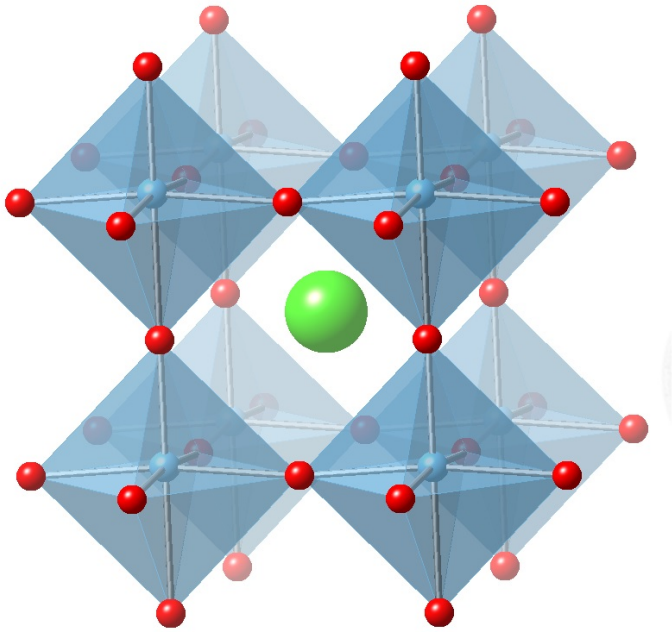

Figure 2.1: Schematic of perovskite structure (ABO_3). A and B are the two cations, and O (Oxygen) is the anion. The atom in the cube center (green) represents the A atom, and the corner atoms (light blue) are the B atoms. Both STO and LAO crystal structure belong to the perovskite family.

Perovskite (ABO_3) thin films are composed of layers of AO and BO_2, which alternate along the 001 direction. In case of STO, the two layers are $Ti^{4+}O_2^{4-}$ and $Sr^{2+}O^{2-}$, with a net charge of zero. For LAO, the two layers are $Al^{3+}O_2^{4-}$ and $La^{3+}O^{2-}$, with net charges of (-e) and (+e) respectively. The close lattice matching of TMO's makes LAO and STO as widely used substrates for the growth of oxide thin films. One of the advantages of using STO as a substrate is the possibility to create a single terminated surface, i.e., TiO_2 or SrO [30, 31]. The treatment process(explained in detail in the next chapter) is of great importance in creating metallic LAO/STO heterostructures. The type of the interface and its physical properties are defined by the type of the substrate termination of the STO substrate. In case of TiO_2 termination(TiO_2-STO), the growth of LAO films starts with a LaO layer, leading to an n-type metallic LaO/TiO_2 interface. As for SrO terminated surface, the growth of LAO starts with an AlO, leading to an insulating p-type AlO/SrO interface. Schematic of the layered structure of a LAO/STO heterostructure with n-type interface (LaO/TiO_2) is shown in Fig.2.2.

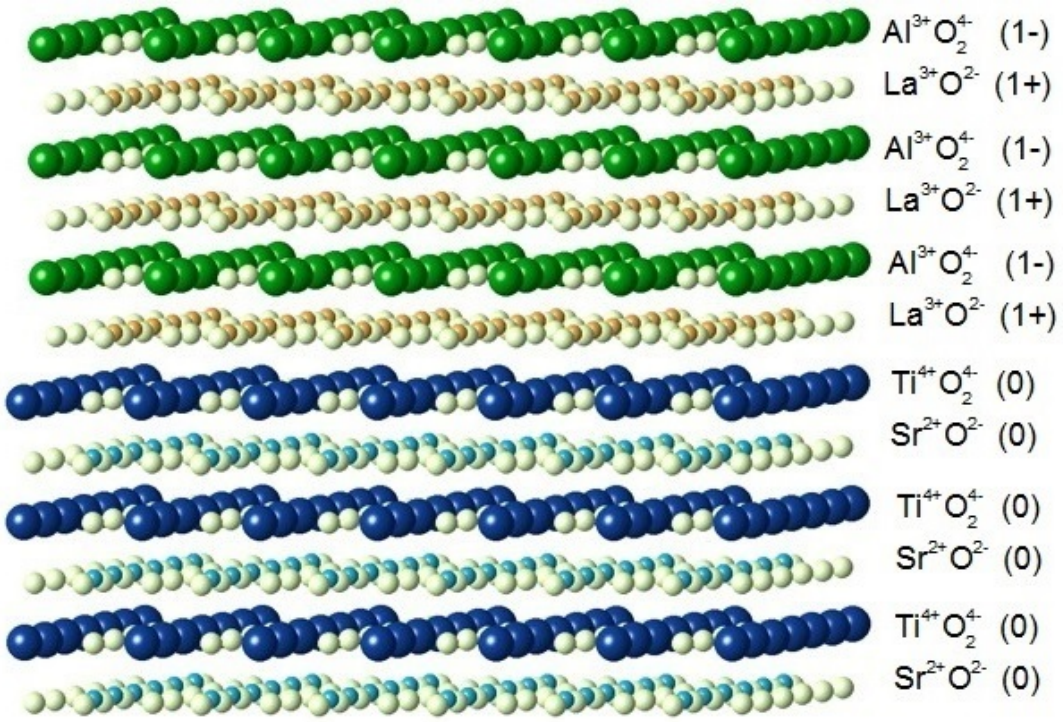

Figure 2.2: Schematic of the layered structure of a heterostructure composed of a LAO thin film deposited on a (001)-oriented TiO_2-terminated STO substrate, which leads to metallic n-type LaO/TiO_2 interface.(Al: green spheres, O: small light green spheres, La: small orange spheres, Ti: blue spheres, Sr: small light blue spheres.)

Due to the difference between LAO and STO lattice constants, LAO films grown on STO experience a tensile strain. The in-plane lattice mismatch ε can be calculated by:

$$\varepsilon = \frac{a_S - a_F}{a_F} * 100\% \tag{2.1}$$

a_S is the lattice constant of the substrate and a_F is the bulk lattice parameters of the film material. For LAO on STO, this results in $\varepsilon = 3.034\%$

2.1.2 Dielectric properties

The STO dielectric properties are important and therefore will be reviewed before investigating the metallic interface properties of LAO/STO heterostructures. The reason is that the carriers responsible for the conductivity in LAO/STO heterostructures reside in Ti-3d orbitals of the STO substrate top layer, which means the interface properties are affected by STO dielectric properties. In this section we will review the dielectric properties of STO, and their dependence on temperature, pressure and electric field. Wang et al. [9] have studied the effect of temperature

and hydrostatic pressure on relative permittivity of STO. The result is shown in Fig.2.3.

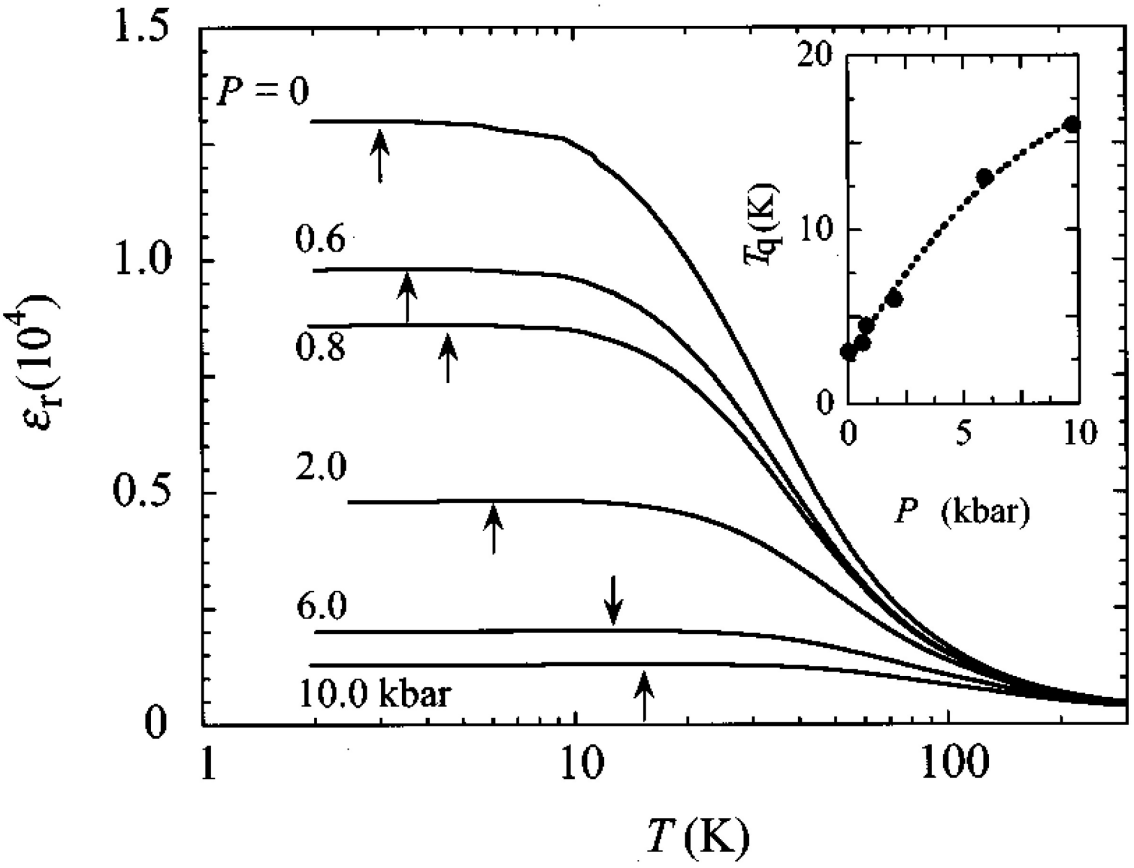

Figure 2.3: Temperature dependence of relative permittivity (ε_r) of STO at different hydrostatic pressure. The figure is taken from Ref. [9]. The transition temperature T_q to a quantum paraelectric state is indicated by arrow. T_q increases with increasing p, see inset.

The relative permittivity ε_r increases with decreasing temperature. The increase is maximum at lower temperature (T<100 K), while at higher temperature, the increase in the relative permittivity is very small. In addition to the temperature dependence of the relative permittivity on temperature, ε_r is strongly affected by hydrostatic pressure. The application of hydrostatic pressure on STO leads to dramatic decrease in ε_r. A hydrostatic pressure of 2 kbar leads to a reduction in ε_r by almost 60% at 4 K(see Fig.2.3). The application of hydrostatic pressure also extends the quantum paraelectric range to a higher temperature [9]. At ambient pressure, ε_r shows Curie-Weiss behaviour down to 15 K, then it becomes constant. In addition to hydrostatic pressure, the relative permittivity of STO is also sensitive to electric field [10]. The relation is shown in Fig.2.4, where ε_r decreases with increasing applied electric field.

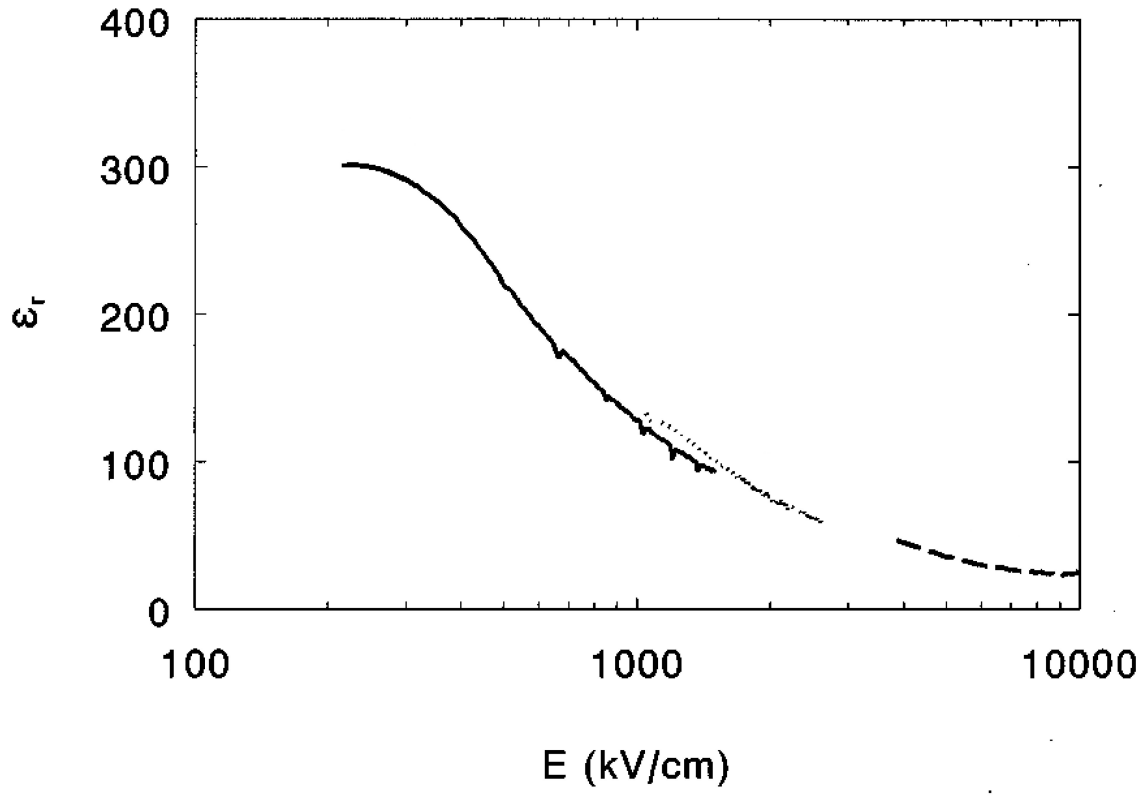

Figure 2.4: Electric-field dependence of relative permittivity(ε_r)of STO. The measurement is done at room temperature. The relative permittivity is decreasing with increasing electric field. The figure is taken from Ref. [10].

2.2 Origin of charge carriers

Different hypotheses have been proposed to explain the origin of the charge carriers in LAO/STO heterostructures. The most important scenarios for the generation of charge carriers are described in the following.

2.2.1 Polar catastrophe

The most common hypothesis used to explain the conductivity in LAO/STO is called "polar catastrophe hypothesis", which was first proposed by Ohtomo el. al. [18] in 2004. It is based on the fact that the polarity (P) of LAO layers generates an electric field (E) within the LAO film, which causes an electrostatic potential (V) which builds up with increasing LAO film thickness, diverging eventually to infinity (see Fig.2.5).

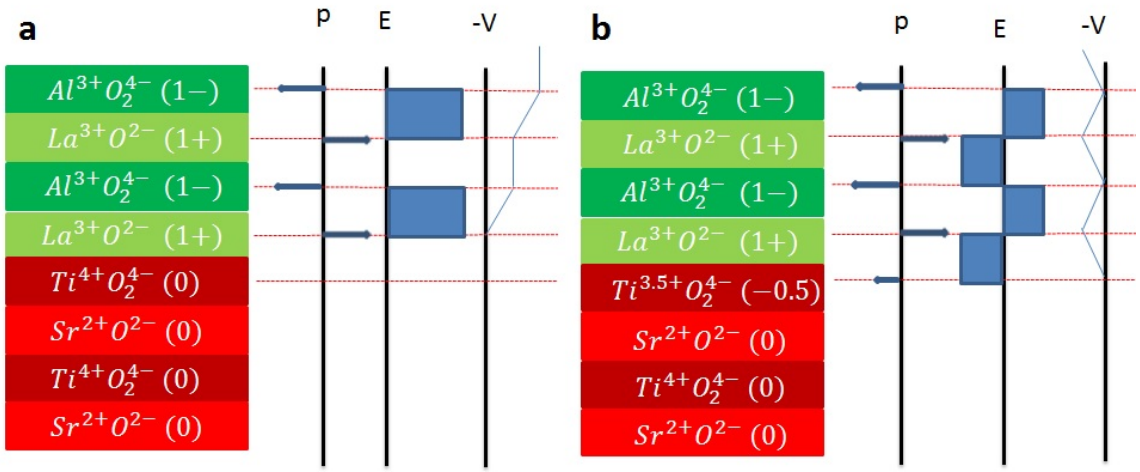

Figure 2.5: The polarity in LAO generates an electric field within the LAO film, which causes the electrostatic potential to diverge to infinity with increasing films thickness, as seen in (a). Once the critical thickness (4 unit cells) of the sample is reached, the potential within the LAO becomes such as high, that half of an elementary charge per unit cell is transferred from the LAO surface to the interface. This reconstruction causes the electric field to oscillate around zero(b) leading to a stable, non-diverging potential.

The polar discontinuity is not restricted to LAO/STO systems. It can also be found in other TMO heterostructures such as, $NdGdO_3$/STO, $GdTiO_3$/STO, $LaTiO_3$/STO and γ-Al_2O_3/STO, and likewise in semiconductors such as, GaAs/Si and GaAs/Ge [32]. There are several ways to avoid the effect of polar discontinuity at the interface. In GaAs/Si and GaAs/Ge, models propose that a roughening at the atomic scale, solves the problem [32]. In case of the LAO/STO interface, a 50% mixed surface termination (TiO_2 and SrO) can also avoid the polar catastrophe. In case of the LAO/TiO_2-STO interface, the build up of the potential causes the energy of the LAO valence bands to increase. That increase in energy causes a charge transfer(half elementary charge per unit cell), from the surface of the LAO film to the interface, specifically to the Ti-3d_{xy} orbitals closest to the Fermi energy E_F. This charge transfer makes the interface to be metallic. The expected sheet carrier concentration of the metallic interface equals to n_s= 3.3x10^{14}cm^{-2} . Polar mismatch is also expected for (111) oriented LAO/STO heterostructure and hence should lead to interfacial doping as well [33].

2.2.2 Oxygen vacancies

The oxygen partial pressure, $p(O_2)$, used during the deposition of oxide thin films, has direct impact on the oxygen content in the film, which crucially affects the film properties. It is well established that LAO/STO electrical properties are very sensitive to $p(O_2)$ used during sample growth [18, 23]. Samples grown at relatively high oxygen pressure $p(O_2) > 0.1$ mbar, are usually

insulating. In contrast, samples grown at lower $p(O_2)$ tend to be metallic. The dependence of conductivity of the samples on the oxygen partial pressure used during film deposition caused speculations that the origin of the charge carriers at the interface is due to the presence of oxygen vacancies (V_O^-)in the sample. The presence of V_O^- results in a reduction of the Ti^{4+} valence-state and hence likewise to the formation of non-localised charge carriers close to the interface.

2.2.3 Ionic intermixing

Another possible source for the generation of electrons at the interface between LAO and STO is atomic intermixing [34, 24]. During sample growth in PLD, atoms/ions with high kinetic energy(some tens of eV) are formed which may penetrate the substrate surface to some extent. This process usually leads to some atomic intermixing in the surface region resulting in a disorder site occupancy. In case of LAO/STO heterostructures, La^{+3} ions may occupy Sr^{+2} sites introducing one extra electron into the electron system. The valency of Ti may also reduce from +4 to +3. However it is doubtful wether the degree of intermixing is strong enough to be considered as a dominant source for free charge carriers in LAO/STO.

The exact contribution from each mechanism mentioned above to the metallic conductivity in LAO/STO is still under debate. It is unclear whether it is possible to create metallic LAO/STO heterostructure where only one of these mechanisms is exclusively present. One rather has to assume that more than one effect contributes to conductivity in LAO/STO. It seems that the polar discontinuity and the oxygen vacancies are the main sources of free electrons in LAO/STO. One can always try to minimize the contribution of oxygen vacancies and ionic intermixing to n_s by carefully controlling the preparation and deposition conditions and analysing their impact on electronic transport properties.

2.3 Electronic properties

Crystal fields cause the degenerate Ti 3d orbitals to split into two e_g and t_{2g} states. Zhong et. al. [11] used density-functional-theory (DFT) calculations to investigate the orbital reconstruction at the interface and found that the t_{2g} orbitals undergoes further splitting caused by the constrained motion of electrons along the z direction which is strongly influenced by the presence of the interface [35]. This splitting in energy at the Γ point was also confirmed by X-ray absorption spectroscopy measurements [19] and by angular resolved photoemission (ARPES) [12], lowering energy of the $3d_{xy}$ orbitals by about 200 meV compared to the degenerate $3d_{yz}$

and 3d$_{xz}$. Fig.2.6 shows the theoretical calculation for the expected orbital reconstruction that occurs at the interface and the ARPES results. The lowering of the d$_{xy}$ orbitals energy is highest at the top layer of STO substrate. As for the layers buried deeper in the STO substrate, the splitting in the Ti-3d orbitals decreases for the layers buried deep in STO substrate, until eventually the orbitals become degenerate again as expected for bulk.

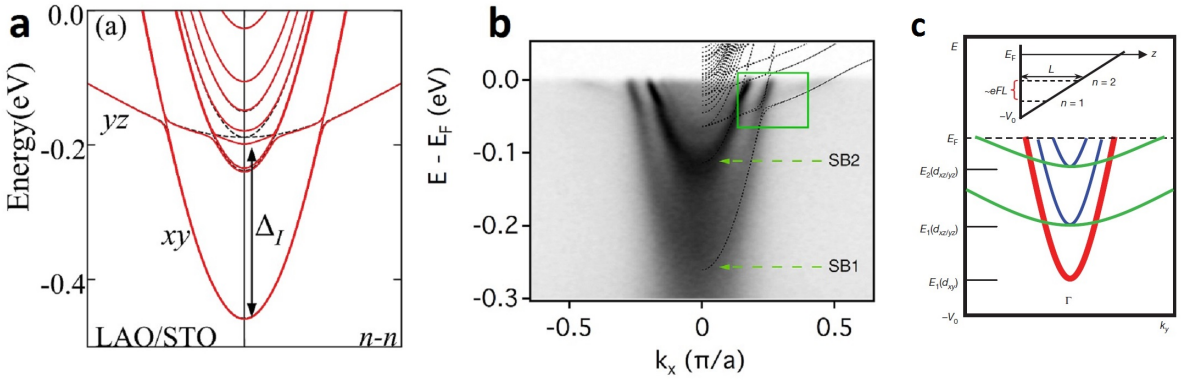

Figure 2.6: a) The DFT calculation for subband structure of LAO/STO heterostructures. The ARPES measurement results (b) of subbands structure of STO(001) surface. The drop in energy of d$_{xy}$ orbitals differes form one layer of STO to another. The highest drop in the d$_{xy}$ orbitals occurs at the top layer of the STO substrate, at the vicinity of the interface. As we dive deeper into the STO substrate, the splitting decreases per layer(c),until it reaches the value of zero, where the three 3dTi orbitals are degenerate again, as it is expected in bulk STO. Figures are taken from [11], [12] and [13].

The difference between 3d$_{xy}$ orbitals and 3d$_{xz}$ and 3d$_{yz}$ is that the former reside in the TiO_2 planes close to the interface, while the latter extend further into STO substrate in the direction perpendicular to the interface. This reconstruction causes the charge carriers to occupy the 3d$_{xy}$ orbitals first. As sheet carrier density increases and a certain charge carrier density is reached (n$_c$ = 1.7x10^{13} cm^{-2}), a Lifschitz transition occurs, i.e., the Fermi-surface symmetry changes due to the additional occupation of 3d$_{xz}$ and 3d$_{yz}$ orbitals, leading to multi-band transport behaviour [15]. Conducting-tip AFM experiment show that the metallic interface has a thickness of about 7nm [36]. The system also exhibits Rashba splitting (splitting of the spin band in two-dimensional systems caused by the existence of spin-orbit coupling along side asymmetry of the orbitals in the direction perpendicular to the two-dimensional system). The splitting energy around the Γ point is only a few meV for 3d$_{xy}$ orbitals. The magnitude of this splitting can be modulated by the application of an external electric field [37].

The system also exhibits two-dimensional superconducting transition with a Berezinskii-

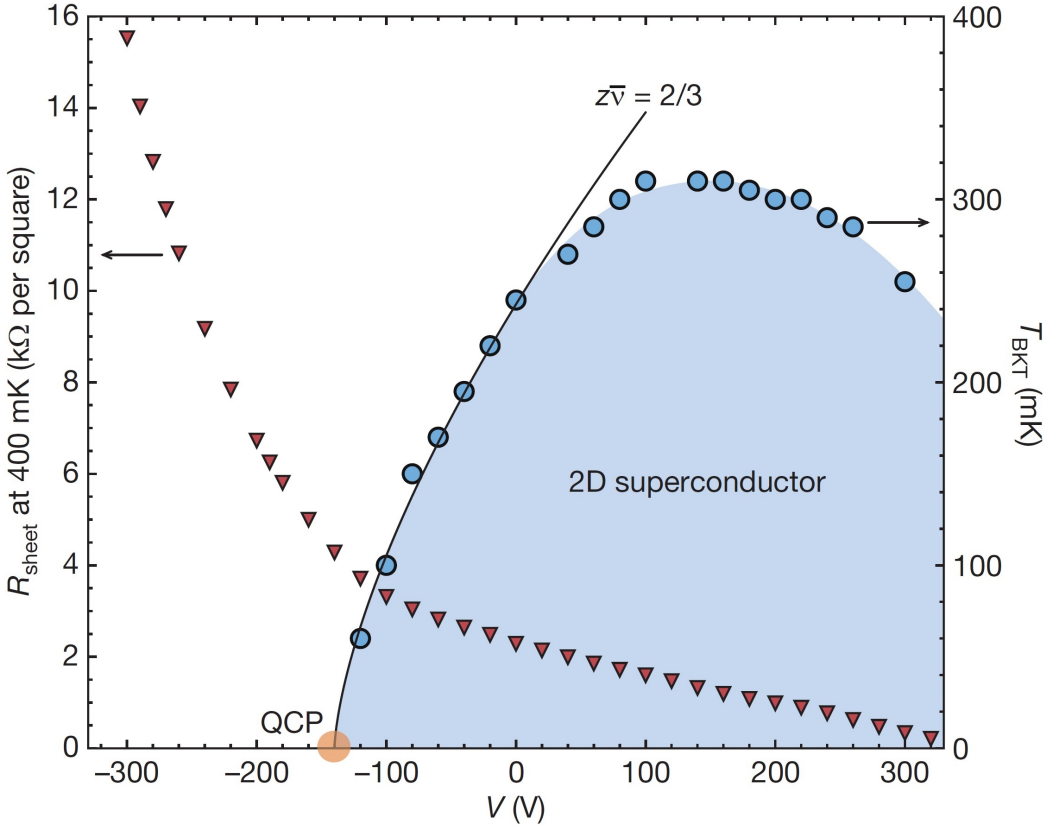

Figure 2.7: Critical temperature T_{BKT} (right axis, blue dots) is plotted against gate voltage. The solid line describes the approach to the quantum critical point (QCP) using the scaling relation $T_{BKT} \propto (V - V_c)^{2/3}$. Figure is taken from [14].

Kosterlitz-Thouless transition temperature T_{BKT} of ∼250 mK [25]. This superconducting transition is found to be sensitive to the charge carrier density at the interface, which can be tuned by applying a back gate voltage to the sample [14]. Tuning the charge carrier density near the superconducting transition temperature allows one to switch back and forth between the superconducting state and the normal state. Fig.2.7 shows the critical temperature T_{BKT} and the sheet resistance R_S dependence on gate voltage. The superconducting region of the phase diagram is mapped by measuring T_{BKT} under different values of applied gate voltages. The maximum value of T_{BKT} amounts to about 315 mK, at gate voltage of about +120 V. A quantum critical point (QCP) can be deduced from the phase diagram using the scaling relation $T_{BKT} \propto (V - V_c)^{2/3}$ [14]. The QCP occurs at n_s= 1.5x10^{-13} cm^{-2}.

Chapter 3

Experimental

3.1 Sample preparation

3.1.1 Substrate treatment

The fabrication of heterostructures and superlattices with full control over their composition and structure at an atomic level is one of the most exciting areas of condensed matter research. Using substrates with atomically flat surface is essential to obtain high-quality thin films. A well defined surface of the substrate enables researchers to fully control the structure of the thin film grown on top of it. One of the most used substrates for growing oxide thin films and heterostructures is $SrTiO_3$. The lattice constant and thermal expansion coefficient of STO is compatible with many interesting TMO's such as high temperature superconducting cuprates. Together with the ability to produce STO in large size single crystals with high purity, made it a popular choice among thin film scientists.

As mentioned earlier, STO has a cubic perovskite structure with lattice constant of 3.905Å. Along the [001] direction, the STO structure can be viewed as alternating layers of a charge neutral SrO layer and a charge neutral TiO_2 layer. STO substrates with different orientations such as (110) and (111) are also widely used. The (110) oriented STO can be built up by alternating $SrTiO^{4+}$ and O_2^{4-} layers while the (111) oriented STO structure can be constructed by alternating layers of SrO_3^{4-} and Ti^{4+} [31]. See Figs. 3.2 and 3.3.

Generally, the surface of as-received (001)-oriented STO substrates contains a mixture of both terminations SrO and TiO_2. By the use of chemical etching, the SrO layer can be removed from the surface. This process consists of chemical and thermal treatments [31, 30] and is routinely used to obtain a TiO_2 termination of (001) oriented STO substrates [38]. In this section,

the termination process of (001), (111), (110) oriented STO substrates is described in detail.

First, the substrate is soaked in ultrasonic bath of distilled water for 10 minutes. The water reacts with the strontium oxide creating strontium hydroxide ($Sr(OH)_2$) at the surface of the substrate.

$$SrO + H_2O \rightarrow Sr(OH)_2$$

After that, the substrate is etched for 30 seconds in a buffered hydrofluoric acid(BHF) solution which removes the strontium hydroxide ($Sr(OH)_2$) from the surface of the substrate. After that, the substrate is annealed under ambient oxygen flow and temperature of 950^oC for 90 minutes. The heating and the cooling rates are set at 200^oC per hour. Fig. 3.1 shows a schematic of the substrate cross section before and after the termination process.

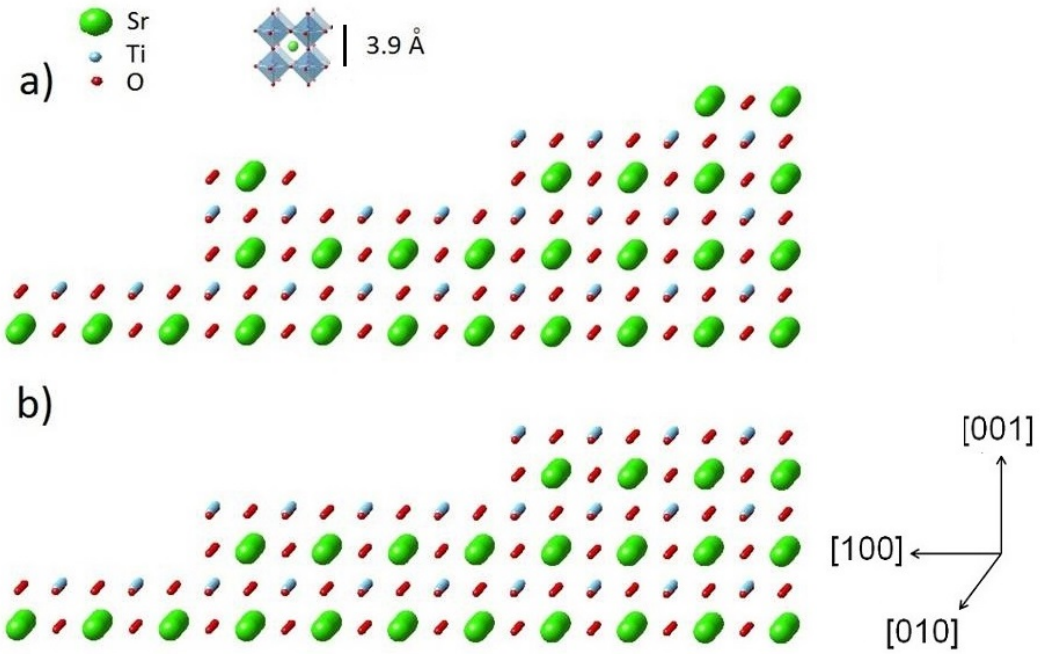

Figure 3.1: A sketch of a (001) oriented $SrTiO_3$ substrate before(a) and after(b) the chemical selective etching. In (a), the surface upper layer has a mixed termination of SrO and TiO_2. After the treatment process, the SrO is removed completely leaving TiO_2 terminated surface.

In order to investigate the surface quality of the treated substrates, we studied the surface by atomic force microscopy (AFM) in contact mode. Fig. 3.2 (a) shows an AFM image of

a treated (001) STO substrate surface (1μm $\times$ 1μm). The surface consists of atomically flat terraces with an average width of about 125nm and a step height of 0.39nm which compares to a single unit-cell height. Hence, the AFM measurements document the single-type termination of STO. For a mixed surface termination a step-height of $a/2$ should be present as well. The average width of the terraces is determined by the miscut angle α, by $\tan(\alpha) = \frac{s}{w}$ where, s is step height and w is the terrace width accounting for α=0.5 for the shown STO substrate.

We can conclude that our (001) substrate is TiO_2-terminated since the TiO_2 layer is stable and does not react with BHF. In order to directly determine the topmost atomic layer of the substrate, time-of-flight mass spectrometry (TOFMS), is usually performed. This technique is capable of high sensitive surface composition analysis. The results show that surfaces of substrates, treated with this method, are homogeneously TiO_2 terminated [39]. X-ray photo-electron spectroscopy (XPS) can also be used to investigate the substrate surface where XPS spectra are taken for Sr 3d, Ti 2p, and O 1s peaks under surface sensitive conditions [38].

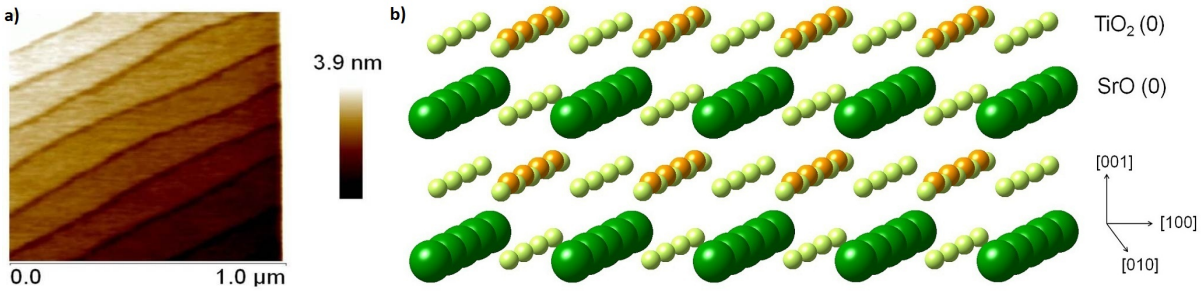

Figure 3.2: (a) AFM scan of (001) $SrTiO_3$ substrate after the TiO_2 termination process. The scan size is 1μm x 1μm. The height of the steps equals to 0.39nm. The terrace width is about 125nm. The crystal structure of a TiO_2-terminated terrace is shown in (b).

In the case of (111) substrates, it is difficult to obtain a well defined surface without atomic reconstruction because of the polar nature of its surface [38]. However, reports have shown that this treatment process is able to produce a well defined surface termination as well. Chemical etching and thermal annealing remove the SrO_3^{-4} layer leaving a Ti-terminated surface.

For (110) substrates, the polarity of the surface is also an issue. Furthermore, the coexistence of Sr and Ti ions on the same plane adds more complexity to the system. Reports have shown that the treatment process results only in a "Ti-rich surface" [39]. The surface terraces are possibly not atomically flat and probably still contain some residual Sr. Therefore, a single-

type termination of (110) oriented STO substrates is usually not possible.

Fig. 3.3 shows an AFM image of a treated (111) substrate and the structure of (111)-oriented STO(b) with a Ti-terminated surface(upper rows).

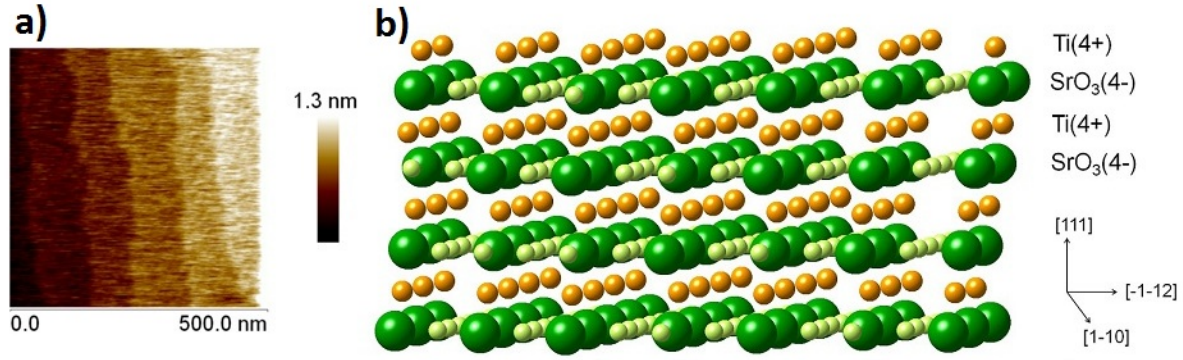

Figure 3.3: (a) AFM image of (111) $SrTiO_3$ substrate surface after the BHF etching process. The image size is 500nm x 500nm. The height of the steps is 2.6Å, and the terrace width is about 100nm. The step height indicates a single-type termination surface(Ti^{+4}). (b) The crystal structure of (111) oriented STO is also shown. The distance between the Ti^{+4} and ${SrO_3}^{-4}$ layers, is a/$\sqrt{3}$=2.25Å.

3.1.2 Film deposition

Pulsed laser deposition (PLD) is considered to be one of the most convenient and reliable methods to produce epitaxial multi-component oxide thin films with very low defect density. The development of this technique started in the 1960s but the major breakthrough came in 1987 when Dijkamp and Venkatesan [40] were able to successfully grow high-quality thin films of (the then newly discovered) high temperature superconductor $YBa_2Cu_3O_7$ using PLD technique. This achievement brought PLD to the spot light and it became a mainstream technology.

In the PLD process, a solid target of the desired film material is exposed to focused high-energy laser pulses in a vacuum chamber, generating a high-temperature plasma which expands away from the target perpendicular to its surface. The material ejected from the target then condenses on a heated substrate located a few centimeters apart from the target. The fast and strong heating of the target surface by the intense laser pulse ensures that all target components evaporate at the same time irrespective of their partial binding energies and individual vapor pressures. This insures that the stoichiometry of the target can be retained to large extent in the deposited films. In fact, preserving the stoichiometry of the target material is the most cited advantage of PLD technique. The laser beam is directed using a set of mirrors to enter the vacuum chamber through a UV-transparent quartz window and is focused on the surface

of a rotating target using a lens. The vacuum chamber is kept at the desired oxygen pressure and at a constant oxygen flow by a set of valves and pumps. The process of the deposition is illustrated in Fig.3.4.

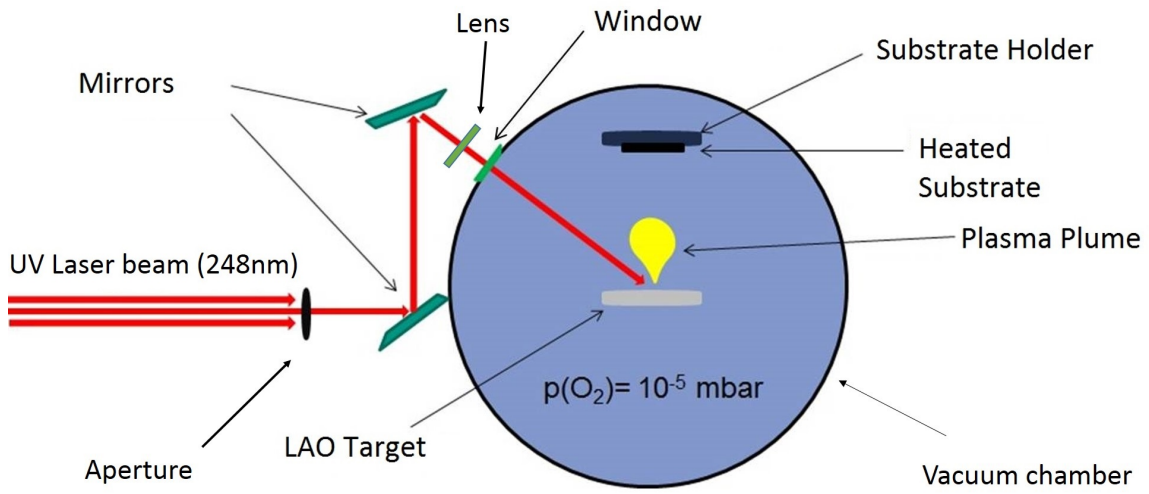

Figure 3.4: Schematic of the process of pulsed laser deposition. The valves and the pumps are not shown in the schematic.

At first glance, the PLD process seems to be very simple and straightforward but, in fact, many variables can affect the film forming process. The laser fluence, pulse frequency, distance between target and substrate, substrate temperature, residual gas pressure, and post deposition annealing time are some of the most important parameters that need to be optimized in order to produce high-quality thin films. In this study, many calibration runs are performed to optimize growth conditions for the production of heterostructures with metallic conductivity and to calibrate the growth rate of the film at these conditions. In the following the optimized growth parameters are described.

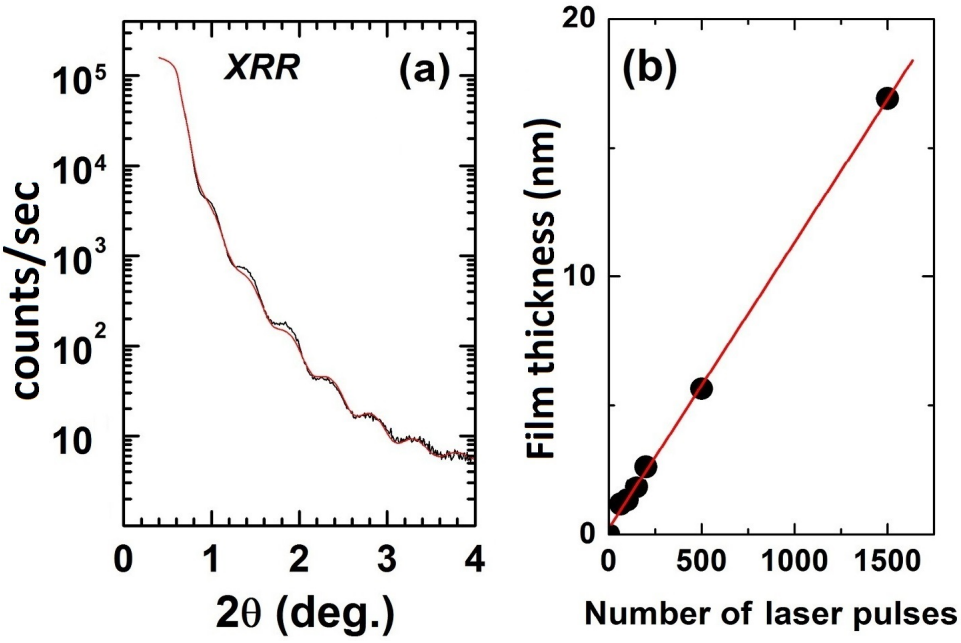

Figure 3.5: (a) X-ray reflectometry measurement for a $LaAlO_3$ film deposited on TiO_2-terminated STO. Simulation of the spectrum(red line) results in a film thickness of d=15nm(40ML) (b) Film thickness as a function of laser pulses. The straight line in (b) is a linear fit to the data from which a deposition rate of 0.11Å per laser pulse is deduced. The thickness of the film is obtained from the reflectometry measurements.

A single crystal of $LaAlO_3$ is used as target to deposit $LaAlO_3$ thin films on TiO_2-terminated $SrTiO_3$ substrates forming $LaAlO_3/SrTiO_3$ heterostructures. The treated substrates are introduced to the deposition chamber where an atmosphere of 10^{-5}mbar oxygen is established. The substrates are then radiatively heated to 650^oC. After that, a UV excimer laser with a wavelength of 248nm is used to ablate the target. The laser fluence is set at 1.1 J/cm^2 with frequency of 2Hz which results in a growth rate of about 0.11Å per laser pulse. After the deposition the film is cooled down to room temperature in $p(O_2)$=10^{-5}mbar. The growth rate is calculated by relating the thickness of a thin film to the number of pulses used to grow it. The thin film thickness can be measured by X-ray reflectivity. Fig.3.5(a) shows an X-ray reflectivity measurement of a LAO film grown on STO (red curve) and the corresponding fit to the data (red curve) from which the film thickness and the roughness can be determined. A plot of film thickness versus number of pulses for a set of calibration runs is shown in (b). In our films the calculated growth rate is 0.11Å per pulse.

3.1.3 Optimization of the oxygen partial pressure

The purpose of the optimization of the oxygen partial pressure $p(O_2)$ is to minimize the number of oxygen vacancies and their contribution to the conductivity in the LAO/STO heterostructures. The optimized $p(O_2)$ is the maximal $p(O_2)$ that can be used during sample growth while maintaining metallic behavior of the sheet resistance down to 4.2 K. We have grown several samples under different $p(O_2)$. Other deposition parameters, such as substrate temperature, laser energy and pulse frequency, were kept constant during the optimization process.

The oxygen partial pressure $p(O_2)$ was varied from 10^{-3}mbar to 10^{-5}mbar. The sheet resistance R_S is plotted in Fig.4.1 versus T for different $p(O_2)$. For $p(O_2) = 10^{-3}$mbar R_S displays a minimum at $T_{MIN} = 47$K. Below this temperature, the sheet resistance increases with decreasing temperature down to 4.2 K. With decreasing $p(O_2)$ T_{MIN} shifts down to lower T, and $R_S(4K)$ decreases considerably from 131k$\Omega/\square$ at 10^{-3}mbar to 200$\Omega/\square$ at 10^{-5}mbar. Only samples grown at $p(O_2)= 10^{-5}$mbar show complete metallic behaviour down to 4.2 K without displaying a minimum in R_S vs T.

To further investigate the influence of oxygen vacancies in the STO substrate on the conductivity of LAO/STO heterostructures, an experiment was performed on a bare STO substrate without material deposition. The substrate was exposed to the same optimized conditions of the deposition process that were used to prepare LAO/STO heterostructures ($T_S = 650^oC$, $p(O_2)$ $= 10^{-5}$mbar), however, without depositing LAO. The STO substrate handled under these conditions were highly insulating down to 4.2 K and did not show any conductivity. So we can rule out, that a significant amount of V_O^- is formed during the PLD process, because of the low $p(O_2)$ used in the process. However, this does not mean, that V_O^- are not present in the samples. The resulting atmosphere may also lead to the formation of reduced Al on top of the STO substrate during the LAO deposition which on the other side may lead to suck out of oxygen from the STO surface. Hence, formation of V_O^- can happen. This process is well known in Al_2O_3 STO heterostructures [41] leading to a reduction of Ti and therefore metallic behaviour.

3.2 Structural properties

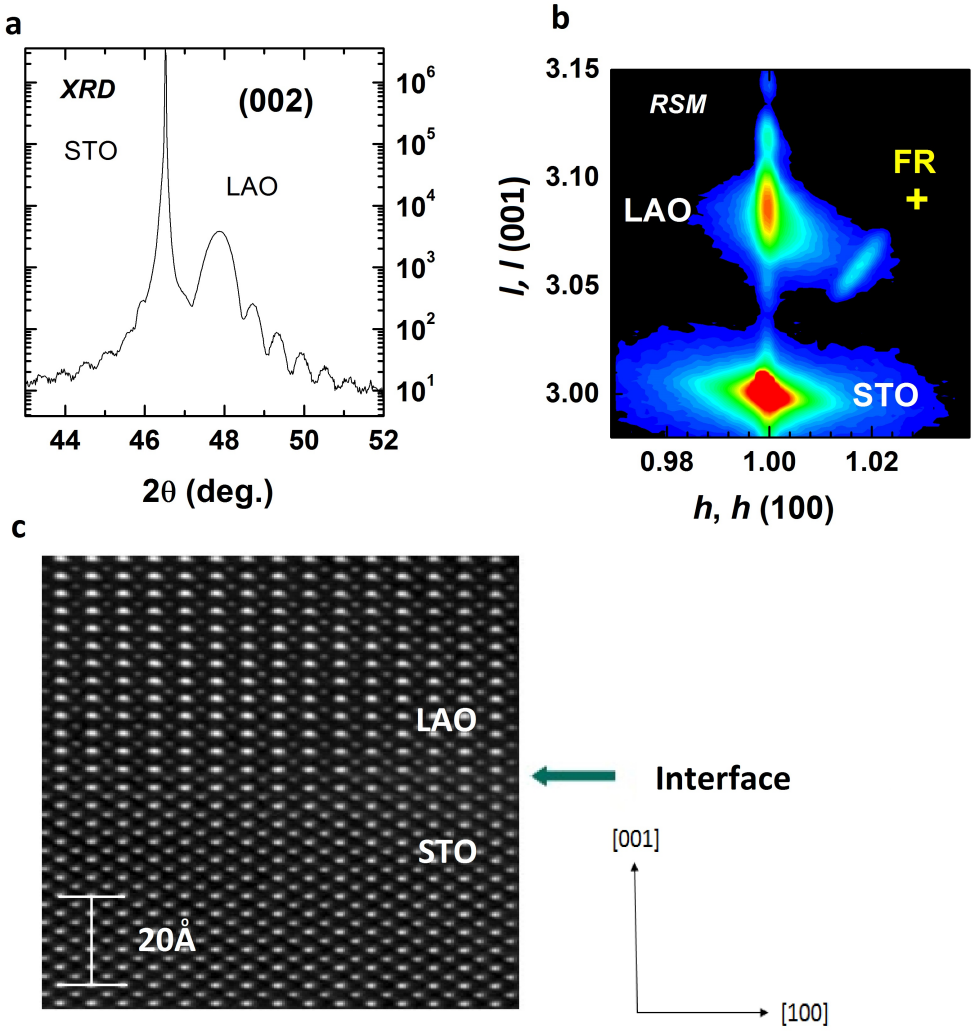

Figure 3.6: (001) oriented LAO/STO heterostructures prepared under optimized growth conditions(see text). The thickness of the LAO layer is 17.9nm (40 monolayers). (a)$\theta/2\theta$ scan in the vicinity of the (002) reflection of STO. (b) Reciprocal space map in the vicinity of the (103) reflection of STO. The contour plot is on a logarithmic scale and shows the scattered intensity as a function of the scattering vector $\vec{q}$, expressed in non-integer Miller indices h and l of the STO substrate reflection referring to the azimuth reference (100) and the surface normal (001). The bright spots indicate the (103) peak positions of STO and LAO from which the in- and out-of-plane lattice parameters are deduced. The cross indicates (103) LAO plane position for fully relaxed(FR) LAO. (c) Spherical aberration-corrected cross-sectional HRTEM of the interfacial region of the LAO/STO heterostructures. Scale and directions are indicated.

Structural properties of the films were investigated by means of X-ray diffraction (XRD) and high resolution aberration-corrected transmission electron microscopy (HR-AC-TEM). XRD measurements were performed using a Bruker D8 diffractometer with CuKα radiation. All samples studied here were grown under optimized growth condition as discussed before in this

chapter. Fig.3.6 (a) shows 2θ-θ scan of a 17.9 nm film which displays a sharp reflection from the (002) lattice plane of the STO substrate at angle $2\theta = 46.5^o$ and to its right, the (002) lattice plane reflection of the pseudocubic/tetragonal LAO film. The high intensity of the LAO (002) Bragg peak, indicates the high quality of the film. The observation of the thickness fringes with high intensities on both sides of the LAO Bragg peak implies good and homogenous crystallinity alike.

The in-plane and out-of-plane lattice constants at room temperature were precisely measured by reciprocal space mapping (RSM). Fig.3.6(b) displays a reciprocal space map of a LAO/STO sample as obtained by X-ray diffraction in the vicinity of the (103) lattice reflection. The LAO film is 40 monolayers thick. As the film thickness (t) increases, the out-of-plane lattice parameter c increases from 3.72Å (fully strained state) and reaches the fully relaxed value of c = 3.79Å for films thicker than 10 monolayers. The in-plane lattice parameter a was found to be always completely strained for all films with thicknesses less than or equal to 40 monolayers i.e., a = 3.9Å which is identical to the lattice parameter of STO.

The microstructural properties of these samples were investigated at the laboratory for electron microscopy in the group of Prof. Dagmar Gerthsen using HRTEM. Fig.3.6 (c) shows a spherical aberration-corrected cross-section TEM image. The image shows a very high crystallinity of the LAO film and a nearly perfect interface between LAO and STO. No significant intermixing of ions (La/Sr or Ti/Al) at the interface was detected. The TEM analysis documents the atomically sharp single-type TiO_2-termination at the interface and high crystalline quality of the prepared LAO/STO heterostructures.

3.3 Dependence of the sheet resistance on the film thickness

The polar catastrophe hypothesis suggests that $LaAlO_3$ films need to have a film thickness of at least 4 monolayers to display a conductive interface. Heterostructures with a LAO layer less thicker are expected to be insulating. Hence, observing metallic conductivity in LAO/STO heterostructures with a LAO thickness less than 4 monolayers suggests that some other mechanisms responsible for metallic behaviour are at work.

For this purpose, $LaAlO_3$ films with different thicknesses were deposited on TiO_2 terminated STO substrates. After the deposition, the sheet resistance was measured at room temperature using the Van-der-Pauw technique. Fig.3.7 shows the room temperature sheet resistance R_S as a function of the LAO film thickness.

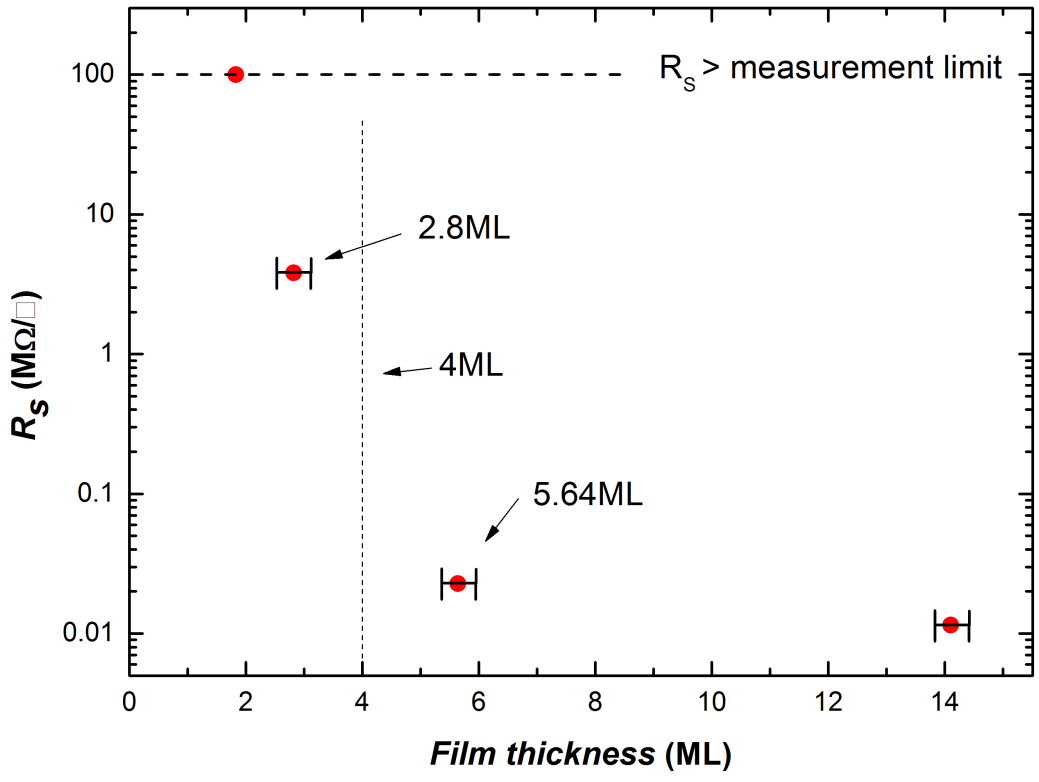

Figure 3.7: Sheet resistance versus film thickness for different $LaAlO_3$ films deposited on TiO_2 terminated STO. The films with thickness below four unit cells are highly resistive. The error bars represent half unit call, which is due to the roughness of the film.

The sample with t=2 ML shows R_S that exceeds our measurement limit. The sample

with t=28 ML has a R_S of 3.76MΩ/□, The sample with t=5.64 ML shows a drastic increase of conductivity with R_S = 22kΩ/□. For LAO films thicker than about 6 ML, R_S seems to saturate at about 11kΩ/□. The most drastic change in conductivity seems to occur between t=3 ML and t=6 ML. The result is consistent with the critical thickness of LAO, i.e., t_{cri}=4 ML, suggested from the polar hypothesis [42].

3.4 Transport measurements under hydrostatic pressure

3.4.1 Pressure cell

The transport properties of the samples were investigated under hydrostatic pressure using a commercial two-layer clamp-type pressure cell from C+T Factory Co.(Tokyo, Japan). The cell has a total length of 70mm and an outer diameter of 25mm. The outer layer is made of CuBe and the inner layer of NiCrAl which enables to reach pressures to about 3 GPa. Inside the cell, a teflon capsule (with an inner diameter of 3.9mm and length of 17mm) is used to host the sample. A schematic of the pressure cell used in this work is shown in Fig.3.8.

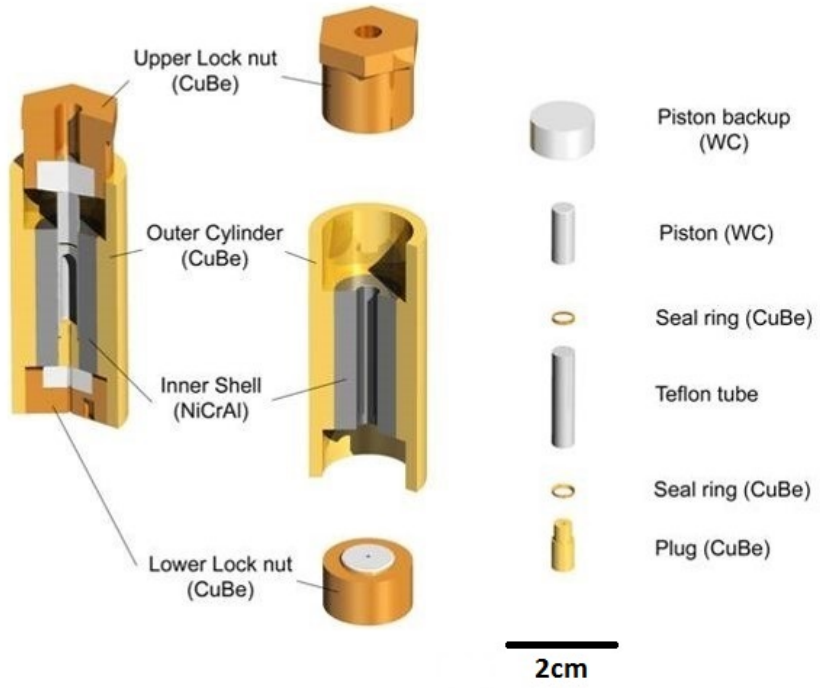

Figure 3.8: A schematic of the pressure cell used in this work. The samples and the pressure gauge (lead piece) were installed inside the teflon tube which was filled with pressure mediating medium. The wires from inside the teflon tube leave the pressure cell from the lower lock nut. The hole in the upper lock nut is used to apply pressure using a rod(not shown) made of tungsten carbide (WC).

The sample (with dimensions $2.5\times2.5\text{mm}^2$) is mounted with its surface normal oriented parallel to the capsule axis within $\pm5^o$. After mounting the sample, the Pb-pressure gauge and the CuBe plug into the teflon capsule, the capsule is filled with a pressure-transmitting medium, namely Daphne 7373 oil (from the company Idemitsu, Tokyo, Japan). This oil ensures approximately hydrostatic pressure up to almost 2 GPa due to its high solidification pressure of

2.2 GPa at 298K [43]. The teflon tube is sealed with a copper beryllium (CuBe) plug. The plug has a small bore hole which allows feeding the wiring to the sample. After feeding all the wires through the copper plug, the bore hole is sealed with a two components glue of Stycast 2651^{TM} and catalyst 9^{TM} (Emerson^{TM} and Cumming^{TM}). The ratio of Stycast to catalyst by weight is 100 to 7. The glue is left for 24 hours to solidify. A hydraulic press is then used to pressurize the cell. With respect to the cross section of the teflon tube (3.9mm diameter), roughly 12kN is needed to achieve a pressure of about 1 GPa. Fig. 3.9 shows the CuBe plug after contacting the sample and a Pb piece serving as a pressure gauge.

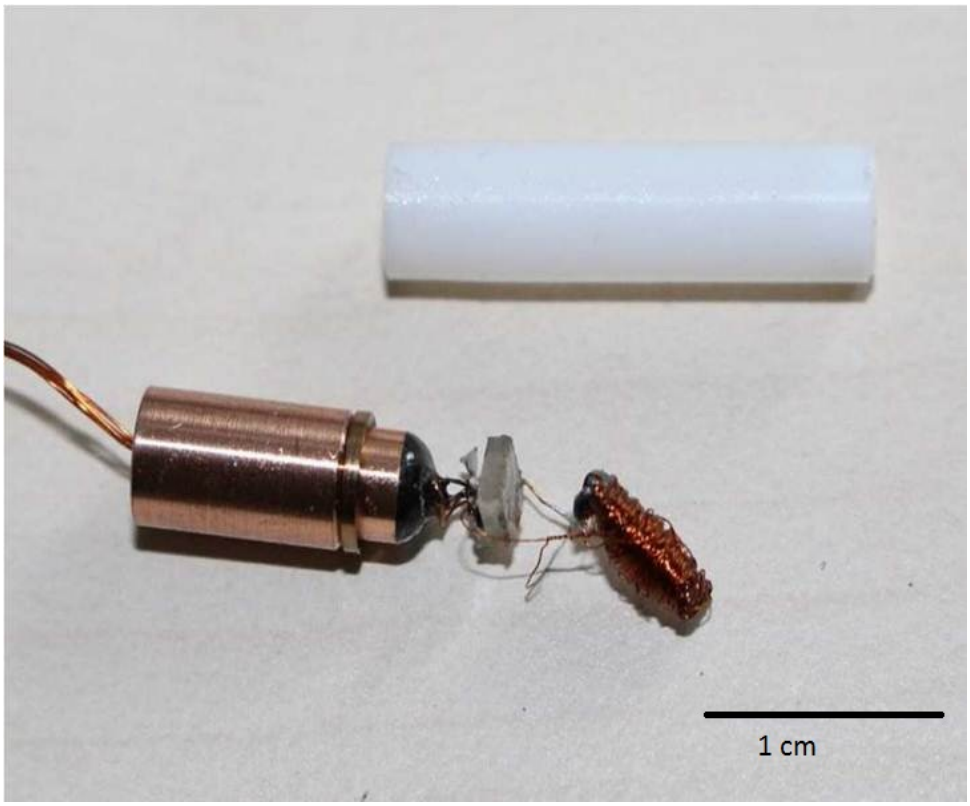

Figure 3.9: The wiring through the copper beryllium plug after contacting the sample and the Pb piece. Both samples and Pb piece are installed inside the teflon tube which is filled with Dalphene 7373 oil as pressure-transmitting medium. The scale is indicated.

All transport measurements were carried out in an Oxford Cryostat. With that cryostat, we are able to measure down to 4.2 K and apply magnetic field up to 7 T. The standard sample holder delivered with the Cryostat was not suitable to host the pressure cell. For this reason, a new sample holder was designed in house. The holder has a tube-like cavity that hosts the pressure cell. After installing the pressure cell in the cavity, a lock nut is used to fix it in place and to prevent it from moving during the measurement. In order to accurately read temperatures and magnetic field during measurements, the temperature and hall sensors of this holder are

installed as close to the pressure cell as possible. Test measurements were carried out to confirm the accuracy of sensor readings of temperature. In these test measurements the pressure cell was filled with Daphne 7373 oil but no pressure was applied and the superconducting transition temperature of the lead piece was measured by an induction method. The measured T_C of the lead piece was 7.2 K which is consistent with literature [44]. This confirms that the readings from the temperature sensor installed on the holder are accurate. Fig.3.10 shows the superconducting transition of the Pb piece measured during cycling the temperature up and down in the vicinity of T_C with a sweep rate of 0.5K/min. The measurement was to account for the delay in temperature acquirement of the cell. The difference between heating and cooling curves is about 17mK. The T_C is determined by taking the average of both curves.

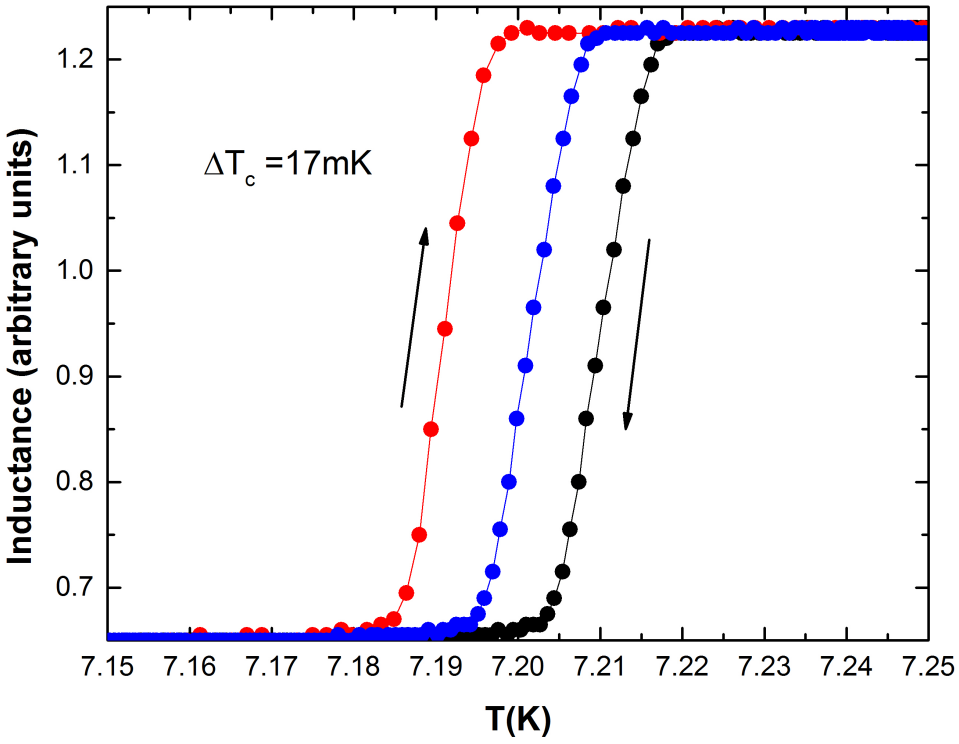

Figure 3.10: T_C measurements of the Pb piece installed in the pressure cell. The teflon tube was filled with Daphne 7373 oil. The pressure cell was sealed before the measurement. The measurements are taken at ambient pressure. For a temperature rate of 0.5K/min, the difference between heating (red symbols) and cooling (black symbols) curves is about 17mK. The blue curve is the average of heating and cooling curves. The unusual sign of the hysteresis might be because the heater position is closer to the lead piece than the thermometer.

For measurements at ambient pressure, a special carrier was used instead of the pressure

cell. Hence, the sample was mounted and contacted on a cylindrically shaped carrier made of copper with the exact dimensions of the pressure cell. The sample was mounted with its surface normal oriented parallel to the cylinder axis alike. A schematic and a photo of the bottom part of the sample holder, pressure cell and sample carrier are shown in Fig.3.11

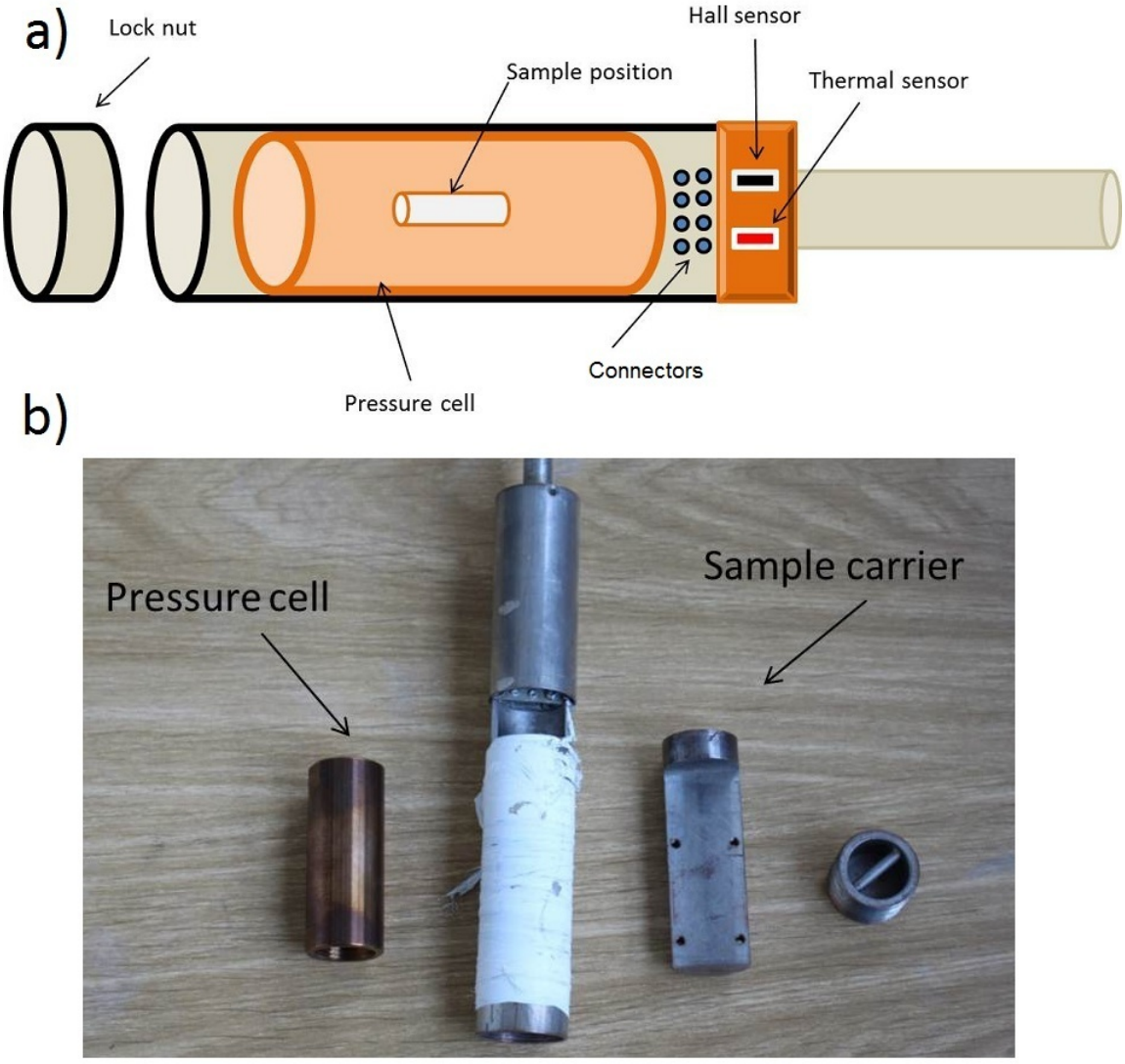

Figure 3.11: (a) Schematic of the sample holder designed to host the pressure cell. The cell is inserted into the tube like a carrier. Hall and temperature sensors are also shown. The sample is located in the center of the teflon tube inside the pressure cell. (b) shows a photo of the pressure cell, the lower part of the sample holder and the sample carrier. The lower part is covered with Teflon tape to protect the wire coiled around the cylinder that works as a resistive heater. The locknut is also shown on the right of the photo, used to close the sample holder after installing either the pressure cell or the sample carrier.

3.4.2 Pressure determination

In order to determine the hydrostatic pressure inside the pressure cell, a piece of bulk Pb is used as a gauge. The large sensitivity of the superconducting transition temperature (T_C) of Pb to the applied pressure (p), i.e., dT_C/dp = -0.365 K/GPa [44], allows for very accurate determination of the pressure. The T_C of the Pb is determined by inductive measurements, where a small coil is wrapped around the Pb piece to pick up the change of magnetic flux induced by its transition to the superconducting state. The coil and the Pb piece are inserted together with the sample inside the teflon capsule. Fig.3.12 shows T_C of Pb at different applied pressures. The uncertainty of the temperature readings is within 17mK(see Fig.3.10), which translates into pressure accuracy of ±0.046 GPa.

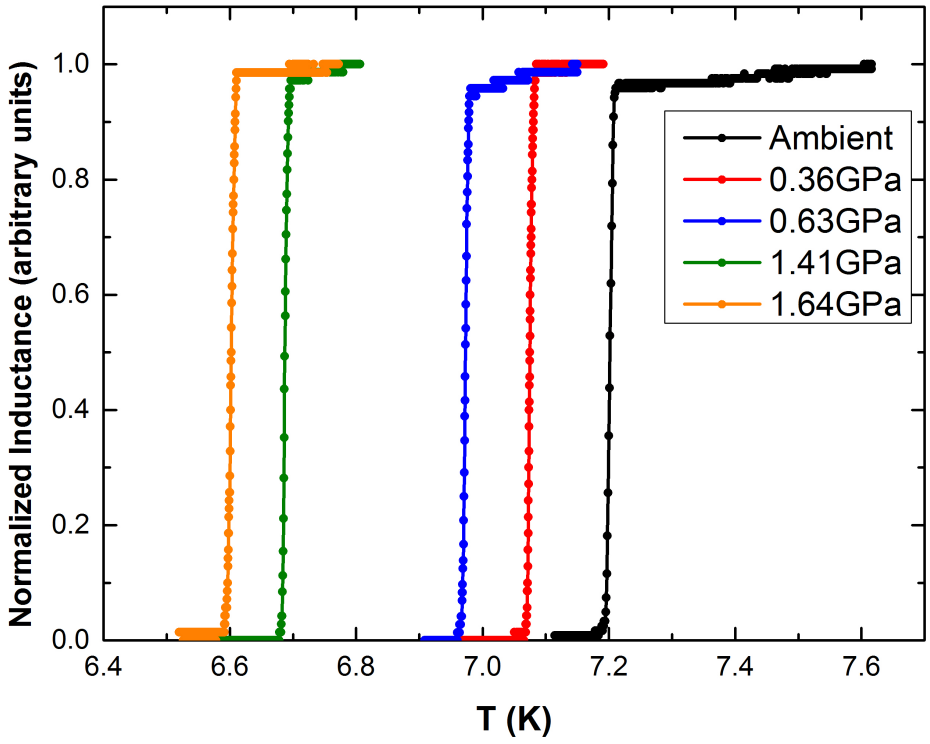

Figure 3.12: Superconducting transition of Pb at different hydrostatic pressure. The data shown here represent the average between the heating and the cooling curves for each pressure.

3.4.3 Contact preparation

Contacts to the sample are made by an ultrasonic wire bonder using a 50μm thick Al wire. This technique commonly achieves good Ohmic contacts to the buried interface. Before bonding, the

film with the standard size of 5 x 5 x 1 mm^3 is cut down to 2.5 x 2.5x 1 mm^3 to fit into the pressure cell. The bonds are placed at the corners of the square shaped sample surface to allow for Van-der-Pauw measurements, which will be discussed in detail in the next section. The bonds are reinforced using silver epoxy glue (EPO-TEK H20E) because of its ability to withstand high pressures. In addition, 0.1mm thick Cu wires are used to further enforce sample contacts(see Fig.3.13). This reinforcement with thicker wires is also necessary to stabilize the sample position within the Teflon tube. The copper wires can be adjusted by bending to achieve the desired orientation and position of the sample. All the wires are fed through the CuBe plug and the lower CuBe lock nut and soldered to the connectors on the sample holder.

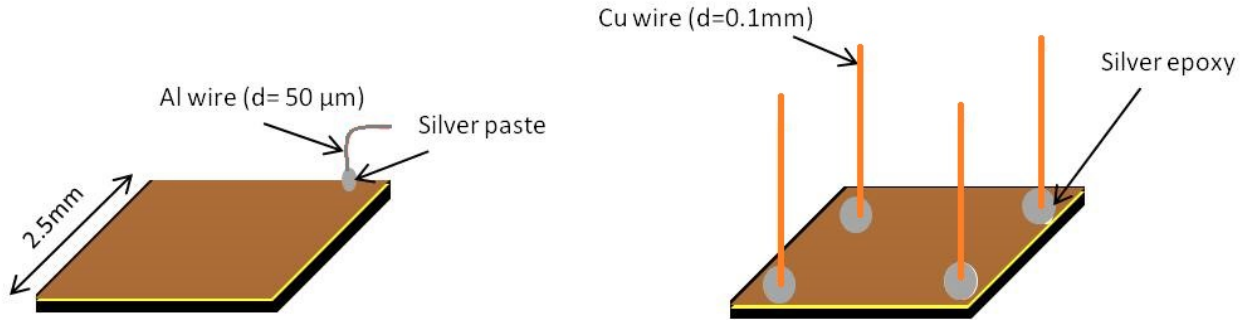

Figure 3.13: Sketch of the contacting process of the buried 2D electron system of a LAO/STO heterostructures using an ultrasonic wire-bonder. Silver epoxy glue and copper wires are used to further enforce the contacts.

To check Ohmic behaviour and stability of the sample contacts we carried out 2 point current-voltage (I-V) measurements. The measurements were done in the range from 1μA to 100μA. The results are shown in Fig. 3.14. The linear behavior of the I-V curve indicates Ohmic behaviour in the used current range. A current of 10μA was used for the transport measurements throughout this work.

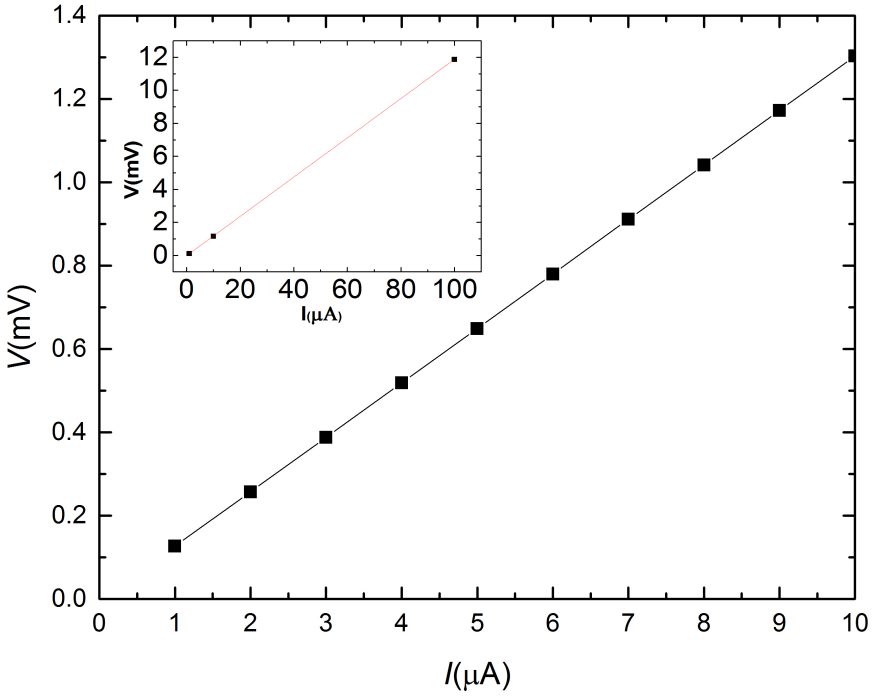

Figure 3.14: 2 point *I*-*V*-measurements performed on a LAO/STO sample after contact preparation (see text). The measurements were done at 4.2 K. The inset represents a linear fit to the data.

3.4.4 Van-der-Pauw technique

Transport properties of the samples are investigated by measuring the sheet resistance R_S, Hall voltage V_H and magnetoresistance MR. All transport measurements are carried out in Van-der-Pauw (VdP) geometry [45]. The square-shaped (2.5x2.5mm^2) of the samples allows for nearly perfect measuring conditions if the contacts for the four-probe measurement are attached to the corners of the sample surface. The VdP technique requires a homogeneous conductivity of the sample with very small thickness. Using conformal mapping, Van-der-Pauw could show:

$$e^{(-\pi d R_{12,34}/\rho)} + e^{(-\pi d R_{23,41}/\rho)} = 1 \tag{3.1}$$

where ρ is the resistivity, d the film thickness and

$$R_{12,34} = \frac{U_{34}}{I_{12}}$$
$$R_{23,41} = \frac{U_{41}}{I_{23}} \tag{3.2}$$

In case of a square shape sample geometry, with the contacts 1-4 at the sample corners(see Fig.3.15)

$$R_{12,34} \approx R_{23,41} \approx R_{34,12} \approx R_{41,23} \tag{3.3}$$

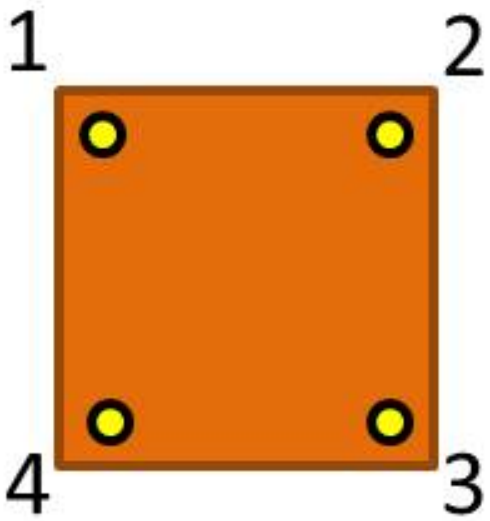

Figure 3.15: Schematic of the geometry used for VdP measurements in this work. The four yellow circles in the corners represent the places where the bonds are made. The sample has dimensions of 2.5mm x 2.5mm. The numbers refer to the contacts in VdP measurement.

The direction of the current is reversed for each measurement in order to remove the effect of the thermoelectric voltages generated at the contacts. These additional measurements increase the total number of measurements for each data point to eight. The average of all eight values gives us R_{avg}.

This simplifies Eq. 3.1 to:

$$\rho = \frac{\pi d}{\ln(2)} R_{avg} \tag{3.4}$$

The sheet resistance R_S is then given by:

$$R_S = \frac{\pi}{\ln(2)} R_{avg} \tag{3.5}$$

For the Hall measurements, the magnetic field B is applied perpendicularly to the sample surface. The Hall coefficient is given by $R_H = \frac{d}{B}\Delta R_{13,24}$. The change in resistance ΔR is measured for positive (+) and negative (-) field direction. We likewise averaged ΔR by $(\Delta R_{13,24} + \Delta R_{24,13})$

$$V_H = \frac{V_{13} + V_{24}}{4} \tag{3.6}$$

Where
$V_{13} = V_{13+}$ - V_{13-}
$V_{24} = V_{24+}$ - V_{24-}

Fig.3.16 shows the negative Hall voltage for a LAO/STO sample under hydrostatic pressure at three different temperatures. The Hall voltage is linear versus the magnetic field up to at least 7 T. This behaviour indicates one type of negative charge carriers. In this case, the sheet carrier density and the Hall mobility can be deduced by: n_s=$\frac{1}{R_H}$ and $\mu_H = \frac{1}{R_s.n_s.e}$. The non-monotonic T-dependence of V_H arises from the non-monotonic $R_s(T)$ dependence (see Fig. 5.1)

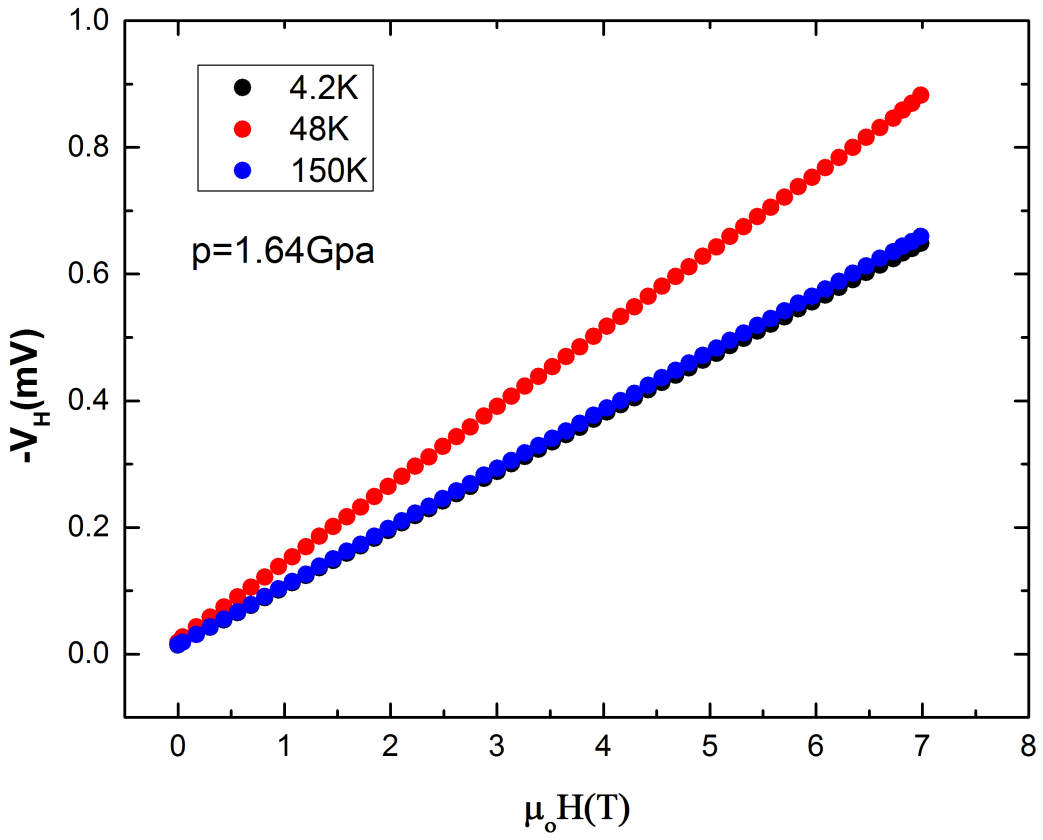

Figure 3.16: The negative Hall voltage versus the magnetic field for LAO/STO. The measurements are taken at p= 1.64 GPa at three different temperatures, T=4.2 K, 48 K and 150 K. The linear behaviour indicates one-type-carrier-transport.

Chapter 4

Electronic transport properties of $LaAlO_3/SrTiO_3$ heterostructures at ambient pressure

4.1 Transport properties of $LaAlO_3/SrTiO_3$ grown under different oxygen partial pressure $p(O_2)$

Transport properties of LAO/STO heterostructure are very sensitive to the oxygen partial pressure during deposition. Generally, the conductivity increases with decreasing oxygen partial pressure [46]. The reason for that is probably that oxygen vacancies in the STO substrate are formed during the deposition process of LAO at low $p(O_2)$ [23]. Oxygen vacancies are a source of electrons in these heterostructures, and can give rise to electrical conductivity. In this chapter, we represent and discuss the sheet resistance (R_S), sheet carrier concentration (n_S)and Hall mobility (μ_H) as a function of the oxygen partial pressure used during sample growth.

4.1.1 Sheet Resistance (R_S)

In Fig.4.1, we have shown the sheet resistance R_S versus T for different $p(O_2)$ ranging from 10^{-5}mbar upto 10^{-3}mbar.

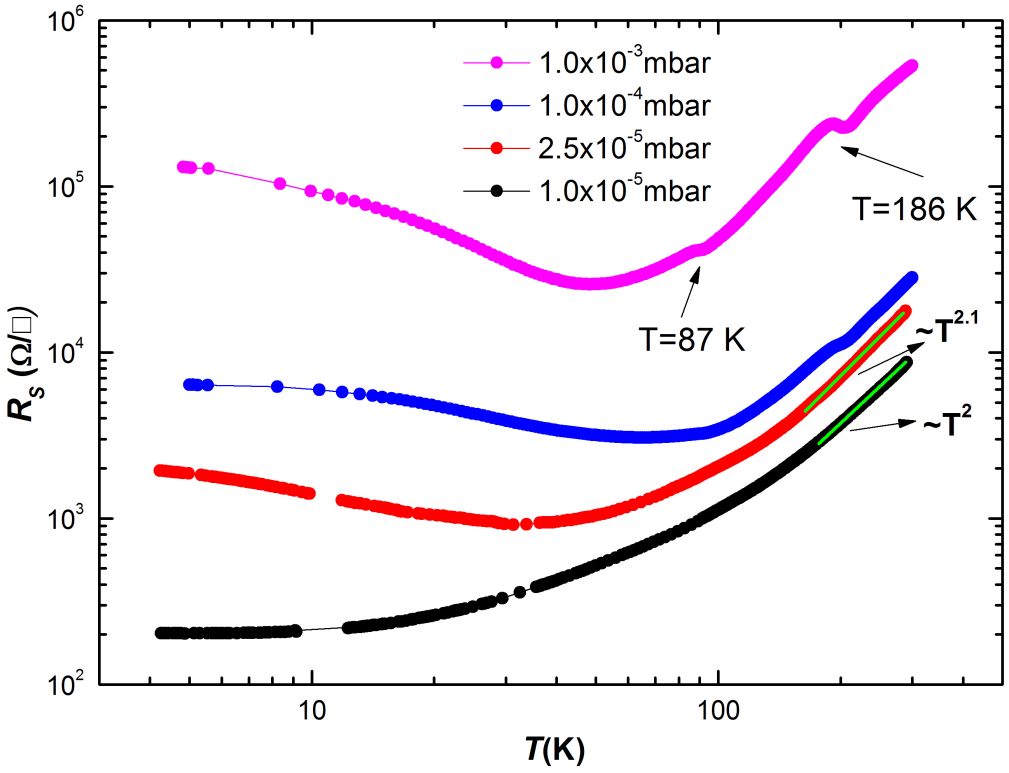

Figure 4.1: The sheet resistance versus temperature on a double-logarithmic scale for $LaAlO_3/SrTiO_3$ heterostructure deposited at different oxygen partial pressure. Increasing $p(O_2)$ used during sample growth results in an increase in R_S. The only sample that shows metallic behaviour down to 4.2 K, is the sample grown at $p(O_2) \geqslant 2.5 \times 10^{-5}$mbar. The green lines represent power law fits to the sheet resistance above 200 K, where the dominant source of resistance is electron-electron scattering.

The sample grown at $p(O_2)$=10^{-3}mbar shows the highest sheet resistance over the whole temperature range. At 4.2 K, the sheet resistance of this sample is about three orders of magnitude higher than the sheet resistance of the sample grown at $p(O_2)$=10^{-5}mbar. For $p(O_2)$= 10^{-4}mbar and 2.5x10^{-5}mbar, R_S amounts to 28kΩ/□ and 17kΩ/□ at room temperature and decreases to 6kΩ/□ and 1.9kΩ/□ at 4.2 K, respectively. Heterostructures grown at $p(O_2)$= 10^{-5}mbar display the lowest R_S, it drops from 8800Ω/□ at room temperature to 203Ω/□ at 4.2 K which gives a ratio of $\frac{R_{s(300K)}}{R_{s(4.2K)}} = 43.35$. At higher temperatures ($T > 200$ K), R_S of samples grown at $p(O_2) < 10^{-3}$mbar shows nearly a T^2 dependence. The green lines in Fig.4.1 represent power-law fits to the sheet resistance for $T > 120$ K. The values of the exponents are 2.1 and 2.0 for $p(O_2)$ = 2.5x10^{-5}mbar and $p(O_2)$ = 10^{-5}mbar, respectively. Van der Marel et. al. [47] argued that electron-phonon interaction leads to a renormalization of the bare electron mass, density of states and plasma frequency by a factor of two, which enhances the electron-electron

scattering, leading to a T^2 behaviour up to 120 K. However, for $T > 100$ K the electron-phonon scattering increasingly contributes to the resistance leading to deviations from the exponent 2.

In addition, samples grown at $p(O_2) > 10^{-5}$mbar exhibit a change to nonmetallic behaviour, i.e. $\frac{\partial R_S}{\partial T} < 0$. The minimum in R_S versus T at $T{=}T_{min}$ changes from sample to sample, and seems not to be dependant systematically on $p(O_2)$. With increasing $p(O_2)$, T_{min} first increases from about 30 K to 50 K. However, for $p(O_2){=}10^{-3}$mbar, T_{min} decreases again to 30 K.

Samples grown at high $p(O_2){=}10^{-3}$mbar show a small dip in the sheet resistance (R_S) at T=87 K and T=186 K. S. Seri et. al. [48] argued that the increase in conductivity at these temperatures is due to the recovery of trapped charge carriers by thermal activation. The trapping of charge carriers, at low temperatures, might be caused by oxygen vacancies [49], by lattice dislocations found in LAO/STO close to the interface [50] or by twin boundaries which may form due to the structural phase transition at $T \approx$105K in STO [51]. Heating the sample close to or above that temperature likely activates charge carriers leading to a lowering of R_S.

4.1.2 Sheet carrier density and Hall mobility

Hall measurements are performed on samples grown at $p(O_2) = 10^{-5}$mbar (Sample A) and $p(O_2) = 2.5 \times 10^{-5}$ mbar (Sample B) in the temperature range from 4.2 to 300 K. The sheet carrier concentration (n_s)and the Hall mobility(μ_H) are deduced as explained before. The results are shown in Fig. 4.2 and Fig. 4.3.

At room temperature, sample A and sample B have a sheet carrier density of $n_s = 1.26 \times 10^{14}$cm^{-2} and 7.3×10^{13}cm^{-2}, respectively. The slight difference in n_s is likely due to the formation of charge carriers as a result of higher content of oxygen vacancies (V_O^-). n_s for both samples decreases with decreasing temperature, as shown in Fig.4.2. The charge-carrier-freeze-out effect might be caused by V_O^- sites, which may act as charge trapping potentials [49]. It is well known that thermal activation of charge carriers is present in LAO/STO heterostructures [48]. The theoretical value of n_s generated at the interface, according to the polar catastrophe hypothesis, is 3.3x10^{14}cm^{-2}, i.e., $e/2$ per surface unit cell. Our results show that n_s of sample A at room temperature is about one third of that value and about one order of magnitude less at 4.2 K. Nevertheless, these observed values of n_s are in good agreement with values reported by other groups [52, 15]. For both samples, $n_s \approx$ 1.7x10^{13}cm^{-2} at 4.2 K, which compares well to the critical sheet carrier density (n_c) in LAO/STO [15], at which the d_{xy} orbitals are nearly completely filled, and d_{xz} and d_{yz} orbitals begin to be occupied, resulting in a one-type

charge-carrier transport for $n_s \leqslant n_c$.

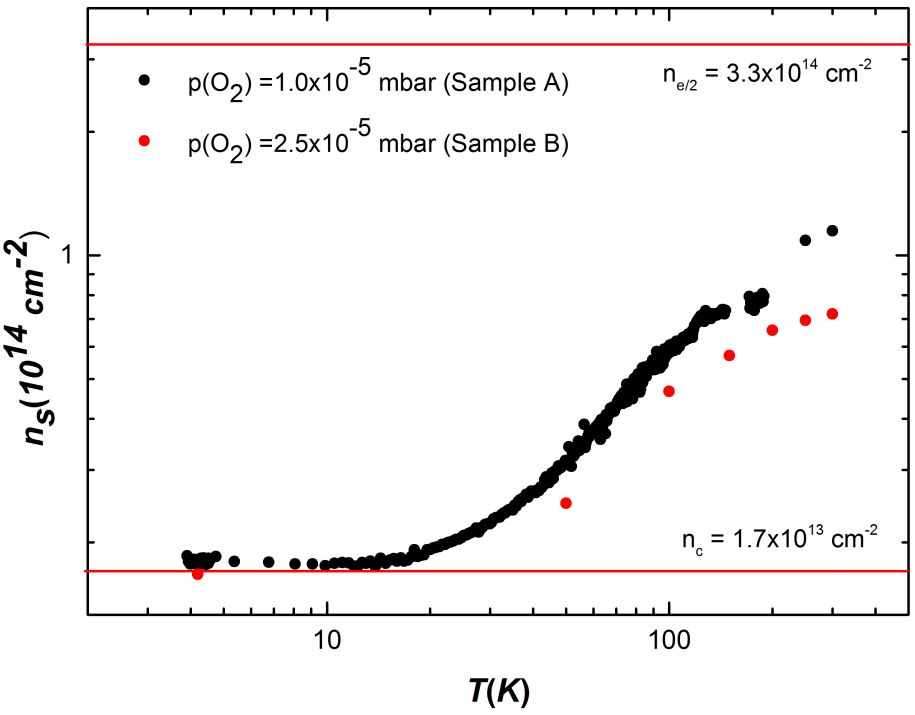

Figure 4.2: Charge carrier density (n_s)of two $LaAlO_3/SrTiO_3$ heterostructures grown at different oxygen partial pressures as a function of T. The lower line in the figure refers to the value of the critical density reported [15], at which a Lifshitz transition is expected to occur. The upper line is the theoretical value of the carrier density expected from the polar catastrophe hypothesis, i.e., $n_s = e/2$ per surface unit cell.

The mobility of the two samples is also deduced form the Hall measurements. The results are shown in Fig.4.3. At room temperature, both samples show the same mobility, which equals to 4 $cm^2V^{-1}s^{-1}$. At higher temperatures (T>50 K), the mobility of both samples displays the inverse T-dependence compared to R_S which is proportional to $T^{-2.2}$. At lower temperatures(T<50 K), sample A shows a higher mobility (1230 $cm^2V^{-1}s^{-1}$) than sample B displaying a mobility of 196 $cm^2V^{-1}s^{-1}$. The increase in the mobility with decreasing temperature is due to the decrease of electron phonon scattering. However, below 50 K, the T-dependence of μ_H no longer follows the $T^{-2.2}$ behaviour, and becomes constant. The change in the T-dependence is related to the domination of impurity scattering, which is expected to be T-independent, resulting in $\mu_H(T) \approx$ constant at low T. Obviously, for T>50 K, electron-phonon scattering is the dominant scattering source, while for T<50 K impurity scattering becomes the dominant source.

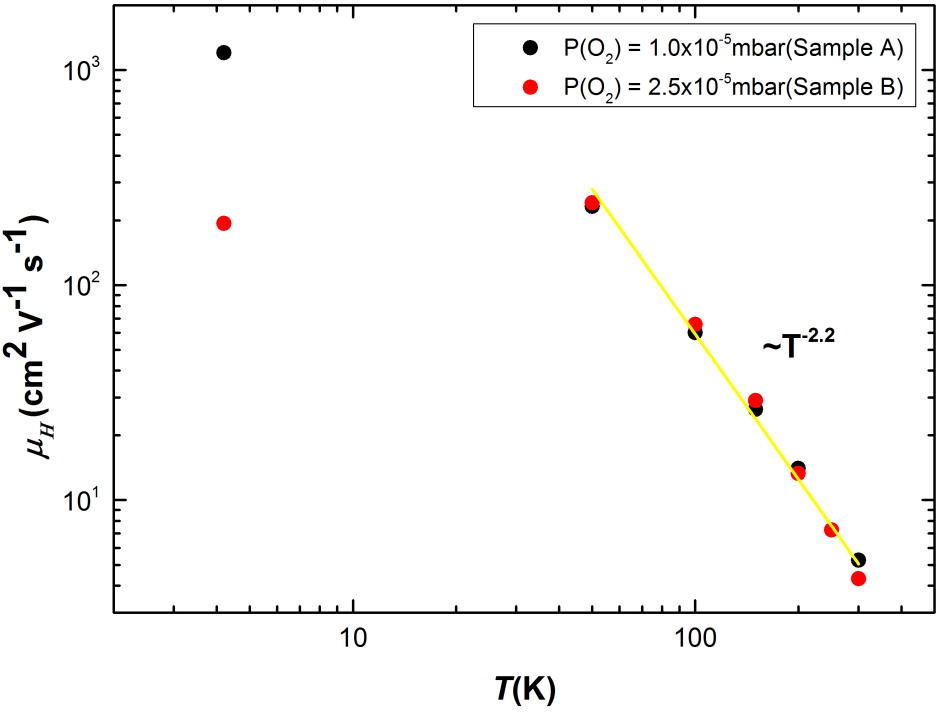

Figure 4.3: Hall mobility versus T of $LaAlO_3/SrTiO_3$ heterostructures grown at different $p(O_2)$. The Hall mobility of both samples decreases with increasing temperature, following a $T^{-2.2}$ dependence for $T > 50$ K, where the dominant source for charge carrier scattering is electron-phonon scattering. The yellow line represents a linear fit to the data for T>50 K.

Chapter 5

Electronic transport properties of $LaAlO_3/SrTiO_3$ heterostructures under hydrostatic pressure

In this chapter, the electronic transport of LAO/STO heterostructures is studied as a function of the hydrostatic pressure applied to the sample. The measurements were carried out from ambient pressure to p=1.64 GPa. Electronic transport was measured as a function of temperature and magnetic field. The samples used in the study were grown under optimized deposition conditions and $p(O_2)$=10^{-5}mbar. Here we focus on the results

5.1 Sheet resistance (R_s)

The sheet resistance for LAO/STO is measured in the temperature range of 4-300 K, under different values of hydrostatic pressure. The results of the measurements are shown in Fig.5.1.

For temperatures T >100 K, the T dependence of R_s seems to depend only minor on hydrostatic pressure displaying roughly a T^2 dependence. The T-dependence in that temperature range is attributed to electron-phonon scattering as discussed in the previous chapter. For temperatures below 100 K, the effect of the pressure on the R_S is more pronounced. R_S at ambient pressure shows metallic behaviour down to 4.2 K. Under hydrostatic pressure, a minimum in R_S at(T_{min}) develops, followed by non-metallic behaviour down to 4.2 K. T_{min} systematically increases with increasing hydrostatic pressure, from T_{min}=34K for p=0.36 GPa, to T_{min}=55K for p=1.64 GPa. R_S at T=4.2 K increases with increasing hydrostatic pressure as well. R_S amounts to 548Ω/□ at ambient pressure and increases to 1.4kΩ/□ at p=0.36 GPa,

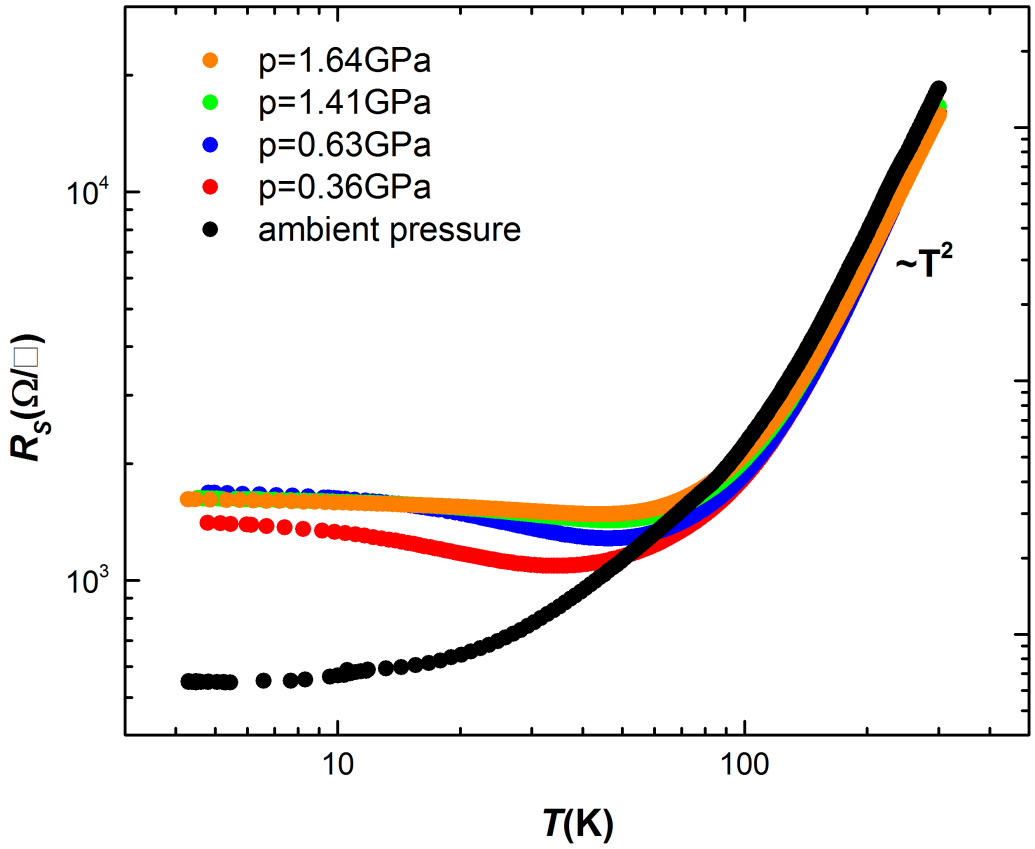

Figure 5.1: The sheet resistance R_s of LAO/STO sample grown under standard conditions as mentioned in chapter 2, under ambient and hydrostatic pressure. R_s at ambient pressure shows metallic behaviour down to 4.2 K. Under hydrostatic pressure, a minimum in R_s develops. Below that, the sheet resistance starts to increase with decreasing temperature.

R_S= 1.6kΩ/□ at p=0.63 GPa and finally seems to saturate at the same R_s for higher pressures.

In the temperature range 10-100 K, R_S is dominated by electron-electron scattering enhanced by electron-phonon interaction (R_{el-el}) and impurity scattering R_{imp}. As demonstrated by van der Marel et. al. [47], R_{el-ph} in STO is well described by a quadratic T dependence, i.e., $R_{el-ph} \propto T^2$ in that temperature range as explained in section 1 in chapter 4. In order to model the impurity scattering, we assume the existence of localized charged impurities that can result, for example, from trapped charge carriers. Oxygen vacancies in STO are known to act as traps for carriers at low T. These trapped charge carriers can be thermally activated when the temperature is close to or above the activation temperature T_A [48, 49]. Once charged, these impurities start to act as scattering centers for free electrons reducing their mobility and hence,

increase R_s. The number of charged impurities as a function of temperature can be described by an Arrhenius law:

$$N(T) = N_o\left[1 - \exp\left(-\frac{T_A}{T}\right)\right] \tag{5.1}$$

T_A is the activation temperature and N_o the total number of charged impurities.

The equation above indicates that the number of charged impurities decreases exponentially with increasing temperature, leading to a reduction of impurity scattering with increasing T. This reduction leads to an increase in carrier mobility, which again reduces R_S with increasing T. In addition to the number of charged impurities, $N(T)$, the magnitude of the scattering potential (V) of the impurities must be also considered. Because of the high dielectric permittivity ε of STO at low T, screening of scattering potentials, i.e. $V \propto \varepsilon^-$ may become very effective below 50 K strongly affecting impurity scattering.

As discussed in chapter 2.1, the dielectric permittivity of STO is very sensitive to hydrostatic pressure at low temperatures, decreasing significantly with increasing hydrostatic pressure [9]. The decrease of ε with increasing p leads to a decrease in screening of the impurity potential. At p=constant, ε decreases with increasing T, leading to an additional reduction in the screening behavior alike. Therefore, the temperature dependence of $\varepsilon(T)$ must also be considered in order to model R_{imp} correctly. As discussed in chapter 2.1, $\varepsilon(T)$ is well described by the Barrett formula [53]:

$$\varepsilon(T) = C\left(\frac{T_1}{2}\coth\left(\frac{T_1}{2T}\right) - T_0\right)^{-1} \tag{5.2}$$

C is the Curie constant, T_1 is the temperature at which the quantum properties of the sample become important and T_0 corresponds to the classical mean-field T_c. To is reported to be [9] strongly sensitive to hydrostatic pressure decreasing from 35K at ambient pressure to zero for p >0.16 GPa.

According to Fermi's Golden Rule, impurity scattering is proportional to the number of impurities and the square of the scattering potential of the impurities:

$$R_{imp} = N \times V^2 \tag{5.3}$$

We assume that the impurity scattering potentials V_o is screened by $\varepsilon(T)$, i.e. $V = V_o/\varepsilon(T)$. The temperature dependence of $R_{imp}(T)$ therefore results in:

$$R_{imp} = A\left[1 - \exp\left(-\frac{T_A}{T}\right)\right]\left[\frac{T_1}{2}\coth\left(\frac{T_1}{2T}\right) - T_0\right]^2 \tag{5.4}$$

where the constant A $=\frac{N_o}{C}$

According to Matthiessen's rule, which can be applied in case of isotropic independent sources of electron scattering, the total resistance is given by the sum of all the partial individual resistance which leads to:

$$R_s = R_{imp} + R_{el-ph} \tag{5.5}$$

and

$$R_S(T) = A\left[1 - \exp\left(-\frac{T_A}{T}\right)\right]\left[\frac{T_1}{2}\coth\left(\frac{T_1}{2T}\right) - T_0\right]^2 + B \times T^2 \tag{5.6}$$

In order to deduce the parameters A, T_A, T_1 and B, we fitted Eq.5.6 to the data $R_s(T, p)$ shown in Fig.5.1 in the temperature range from 10-100 K. The fitting results are shown in Fig.5.2

to Fig.5.6. The partial contributions to R_S, R_{imp} and R_{el-ph}, are plotted herein for better comparison over the complete measured temperature range. The T-dependence for T>100 K of R_{imp} and R_{el-ph} were assumed to be the same as given in Eq.5.6.

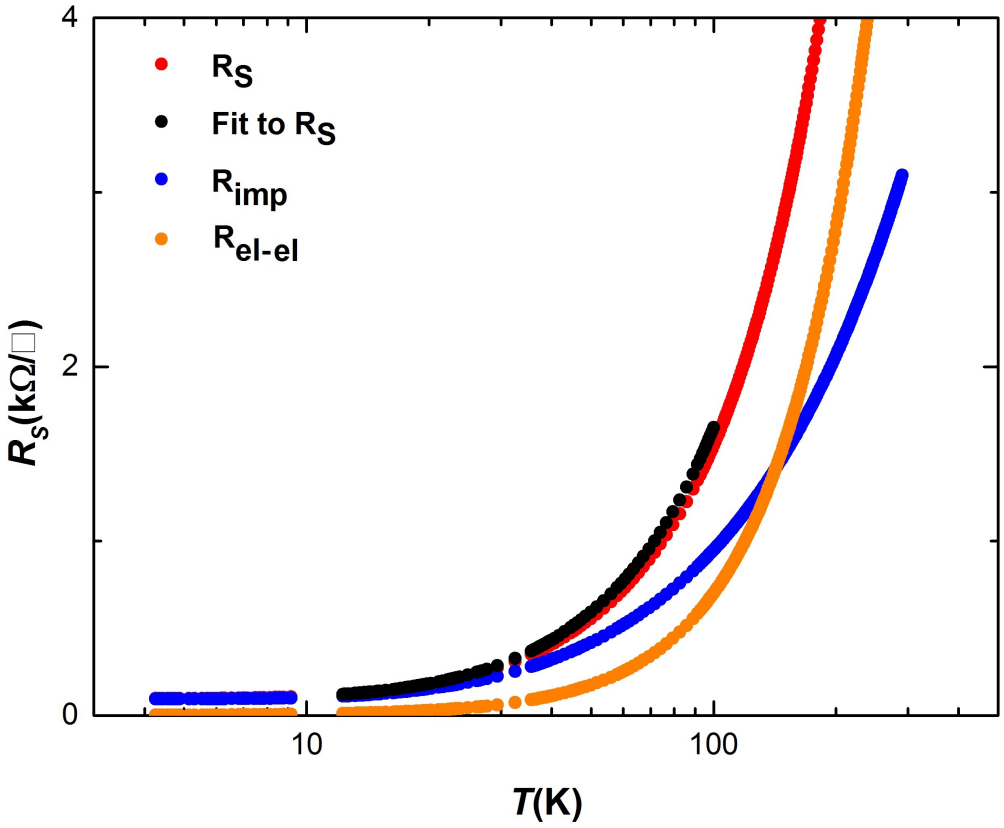

Figure 5.2: Experimental data R_s (red symbols) of the LAO/STO sample under ambient pressure. A fit(black symbols) to the data and the deduced partial contributions to R_s, i. e., R_{imp}(blue symbols) and R_{el-el}(orange symbols) are displayed alike. The T dependence of R_{imp} and R_{el-el} was assumed to be the same over the complete temperature range.

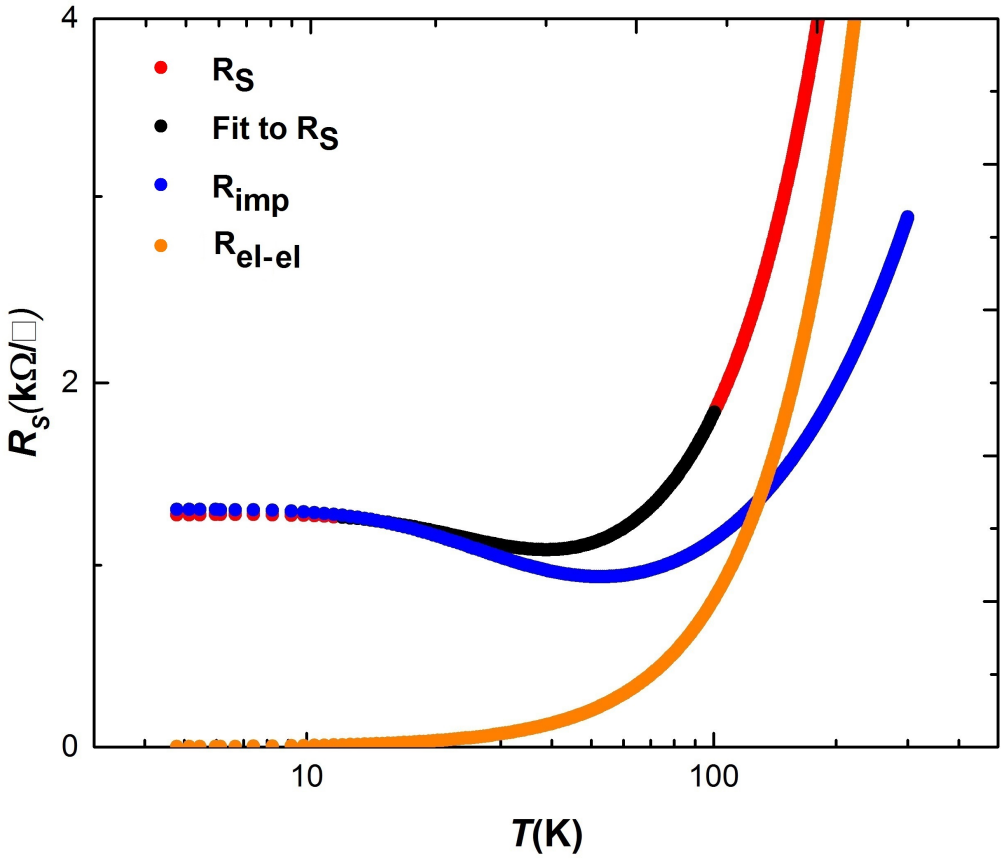

Figure 5.3: Experimental data R_s (red symbols) of the LAO/STO sample under p=0.36 GPa. A fit(black symbols) to the data and the deduced partial contributions to R_s, i. e., R_{imp}(blue symbols) and R_{el-el}(orange symbols) are displayed alike. The T dependence of R_{imp} and R_{el-el} was assumed to be the same over the complete temperature range.

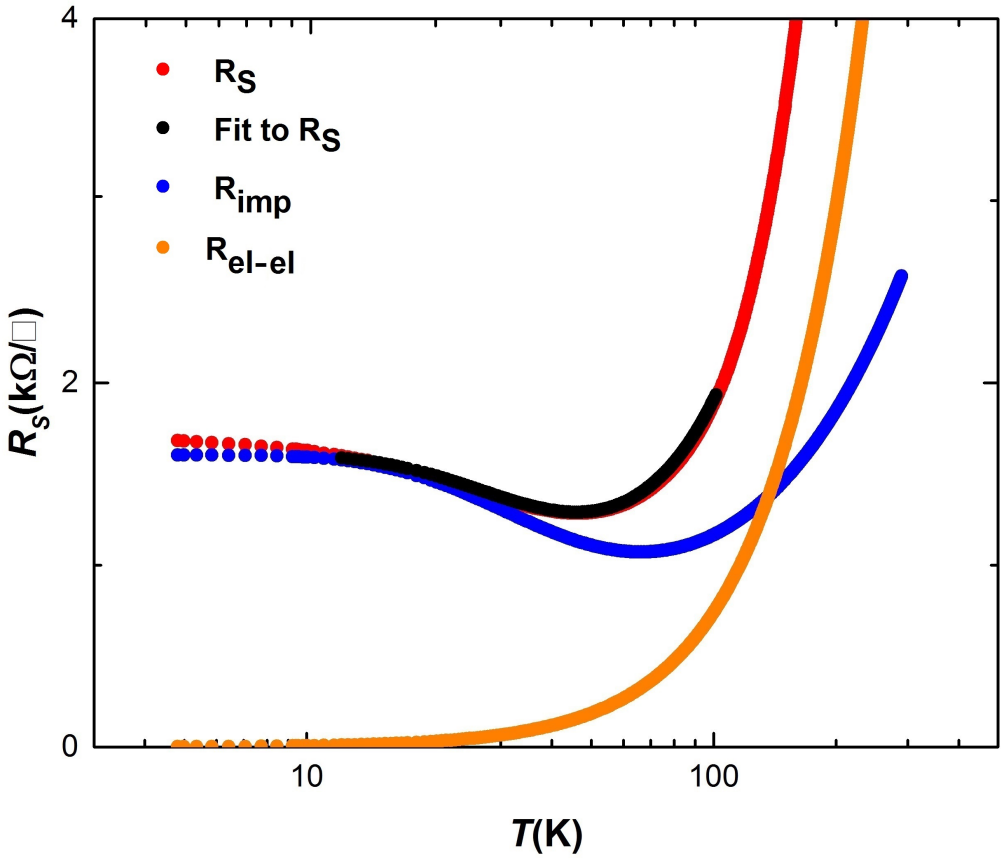

Figure 5.4: Experimental data R_s (red symbols) of the LAO/STO sample under p=0.63 GPa. A fit(black symbols) to the data and the deduced partial contributions to R_s, i. e., R_{imp}(blue symbols) and R_{el-el}(orange symbols) are displayed alike. The T dependence of R_{imp} and R_{el-el} was assumed to be the same over the complete temperature range.

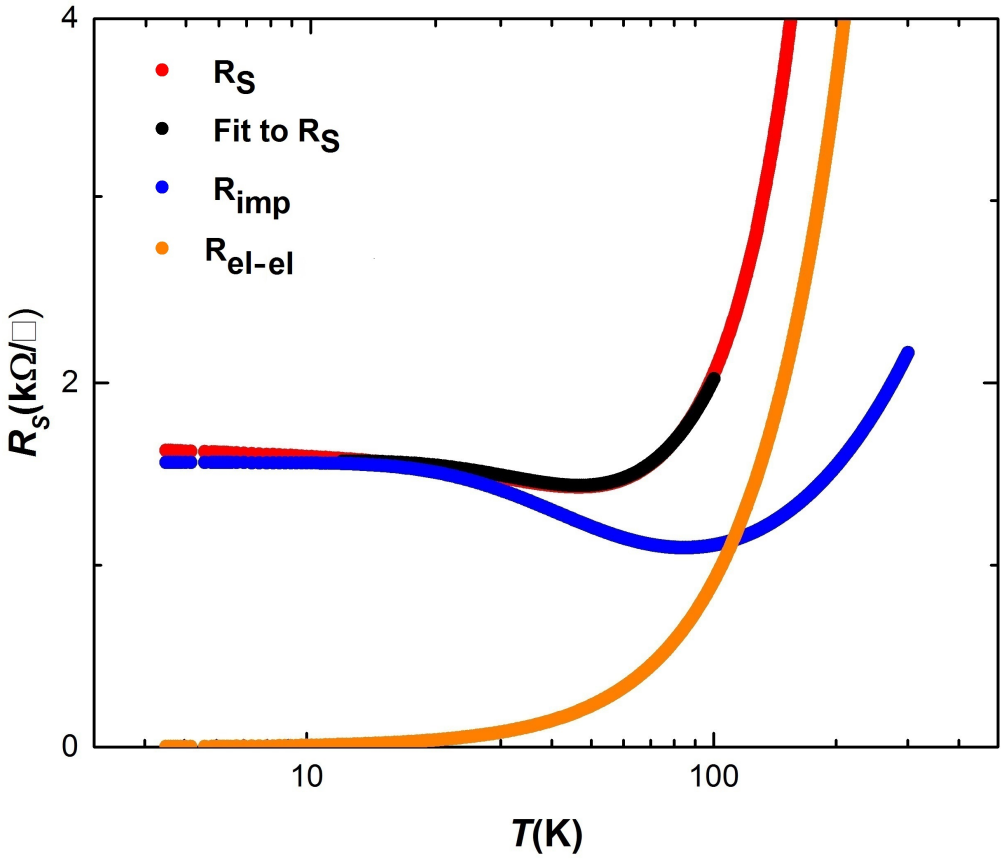

Figure 5.5: Experimental data R_s (red symbols) of the LAO/STO sample under p=1.41 GPa. A fit(black symbols) to the data and the deduced partial contributions to R_s, i. e., R_{imp}(blue symbols) and R_{el-el}(orange symbols) are displayed alike. The T dependence of R_{imp} and R_{el-el} was assumed to be the same over the complete temperature range.

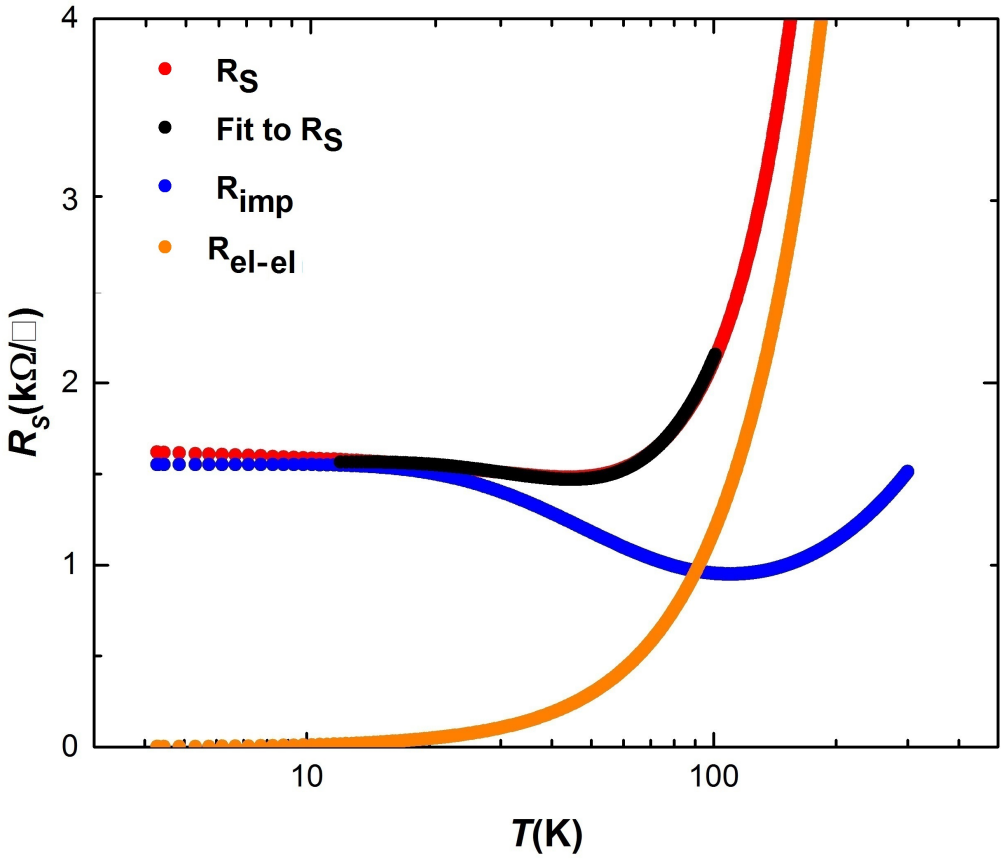

Figure 5.6: Experimental data R_s (red symbols) of the LAO/STO sample under p=1.64 GPa. A fit(black symbols) to the data and the deduced partial contributions to R_s, i. e., R_{imp}(blue symbols) and R_{el-el}(orange symbols) are displayed alike. The T dependence of R_{imp} and R_{el-el} was assumed to be the same over the complete temperature range.

The parameters obtained from the fit of equation 5.6 to the data of $R_s(T,p)$ are given in Table 1.

Table 1: The parameters extracted from fitting $R_s(T,p)$ to Eq.5.6.

p(GPa)	T_A(K)	$A(\Omega/\mathrm{K}^2)$	T_1(K)	$B(\Omega/\mathrm{K}^2)$
Ambient	44	0.26	38.2	0.07
0.36	44	0.23	149.5	0.07
0.63	49.6	0.18	189	0.07
1.41	67.8	0.1	245	0.09
1.64	75.2	0.07	299	0.11

At ambient pressure, T_A amounts to 44 K. Similar activation temperatures for charge carriers were also reported. [48, 49]. T_A increases with pressure to 75K at p=1.64 GPa. T_1, the transition to the quantum paraelectric state, increases from 38.2 K at ambient pressure to 299 K at p=1.64 GPa. An increase of T_1 with increasing p was also reported [9]. The parameter A steadily decreases with increasing pressure which is likely related to a decrease of the Curie-constant under pressure. The parameter B, related to the strength of electron-phonon interaction increases only slightly with increasing p.

Comparing R_{imp} and R_{el-ph} for p larger than ambient pressure, a striking feature is that in contrast to the monotonic increase of R_{el-ph} with increasing T, R_{imp} displays a pronounced minimum in the temperature range from 50-100 K.

That minimum is obviously the reason for the minimum in $R_s(T)$ and caused by the different temperature dependence on $N(T)$ and $V(T)$ determining R_{imp} (see Eq. 5.3.) $N(T)$ decreases with increasing T, whereas $V(T)$ increases. To document the different T dependence on $N(T)$ and $V(T)^2$ determining the T dependence of $\mathrm{R}_{imp}(T)$, we have plotted in Fig.5.7 the normalized number of impurities, $N(T)/N_o$=$\mathrm{N}_N(T)$, and the squared inverse of the normalized permittivity $(\varepsilon(T)/\varepsilon(4.2\ \mathrm{K}))^{-2} = \varepsilon_N^{-2}$ as a function of T for p=0.36 GPa and p=1.46 GPa.

The temperature that marks the onset of a significant T dependence of $N_N(T)$ and $\varepsilon_N^{-2}(T)$ is defined by T^* and T_q, respectively. In case of T_q>T^*, the T-dependence of R_{imp} is controlled by $\mathrm{N}_N(T)$ for T<T_q, i.e., decreases above T^* with increasing T. However, due to the stronger increase of ε_N^{-2} with increasing T above T_q, $R_{imp}(T)$ is controlled by the T-dependence of ε_N^{-2}, i.e., increases with increasing T, therefore leading to a minimum in R_{imp}.

T^* and T_q obviously depend very sensitively on p versus the parameters T_A and T_1 (see Table.1). With increasing p, T^* and T_q shift to higher temperature leading to a shift of the minimum of $R_{imp}(T)$ and hence $R_S(T)$, alike.

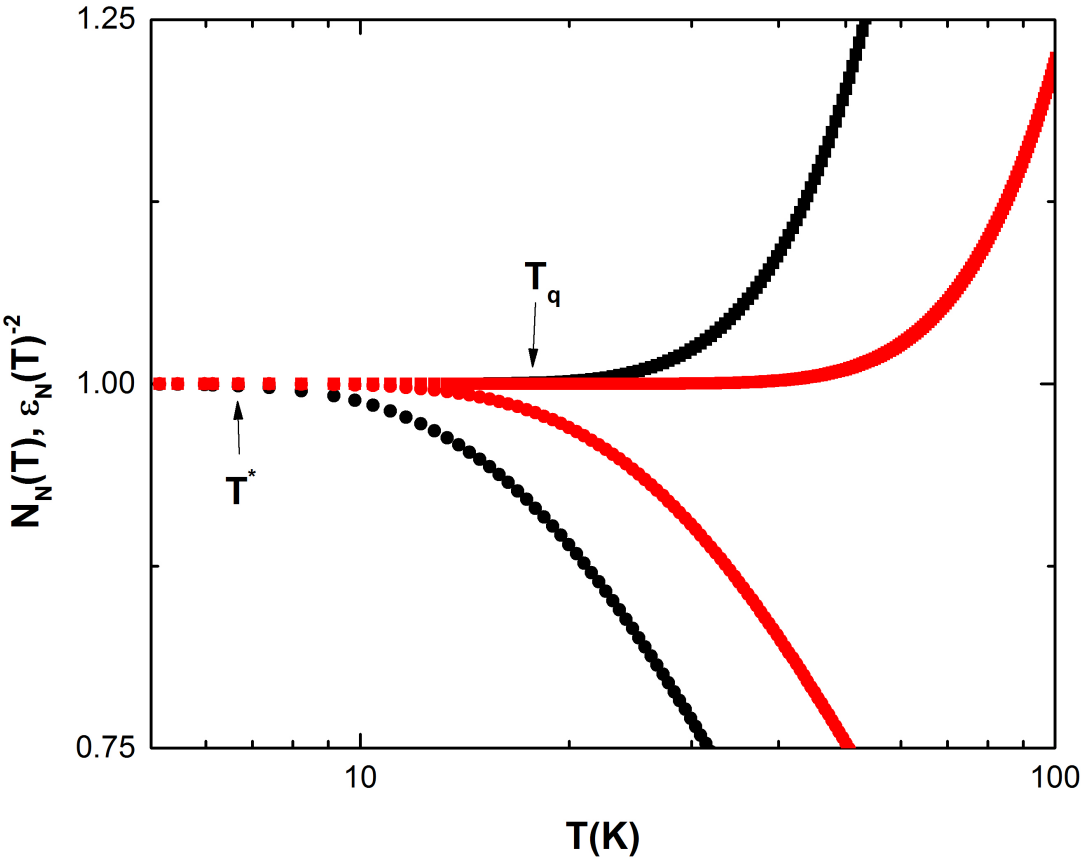

Figure 5.7: N_N(T)(circles) and $\varepsilon_N(T)^{-2}$(squares) as a function of T for p=0.36 GPa(black symbols) and p=1.46 GPa(red symbols). For $T>T^*$ and $T > T_q$, N_N(T) and $\varepsilon_N(T)^{-2}$ become T-dependent, respectively. Both T^* and T_q shown for p=1.46 GPa increase with increasing hydrostatic pressure.

ε_N^{-2} not only increases with T, but also with increasing p. The quite strong p dependence of $\varepsilon(T,p)$ enters the permittivity via the pressure sensitivity of the quantum paraelectric state. As displayed in Table.1, the transition temperature T_1 to the quantum paraelectric state shows strong p-dependence affecting ε directly, i.e. $\varepsilon \propto T_1^{-1}$.

In order to demonstrate the p dependence of $\varepsilon_N^{-2}(T)$ we have plotted in Fig.5.8 $(C/\varepsilon(T))^2$ versus T for different hydrostatic pressure. The curves were generated using the parameter T_1 as deduced from experiment(shown in Tab.1). The p- and T-dependence is well comparable to that reported in [9] for bulk STO. $\varepsilon(p,T)^{-2}$ increases with increasing p, where the sensitivity to

p, $\frac{\partial \varepsilon^{-2}}{\partial p}$, seems to decease with increasing p.

Coming back to $R_s(T,p)$, in the low-temperature range T<10 K, the extrapolation of the fitting curves indicates nearly T-independent behaviour, where $R_s(T,p)$ shows a small increase with decreasing T, which is obviously not described by Eq. 5.6. This will be discussed in more detail in chapter 5.3.

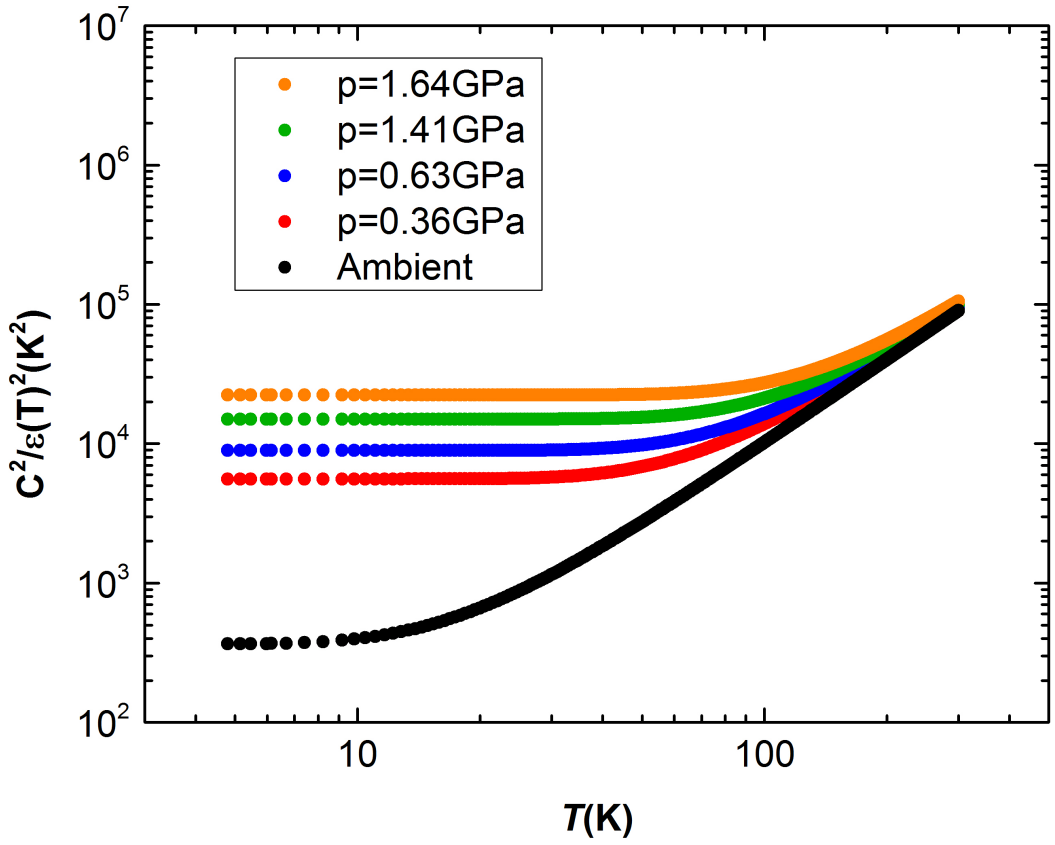

Figure 5.8: $C^2/\varepsilon(T)^2$ versus temperature at different hydrostatic pressure. The curves are generated using the parameter T_1 as deduced from experiment shown in Table 1. The p- and T-dependence is well comparable to that reported for bulk STO [9].

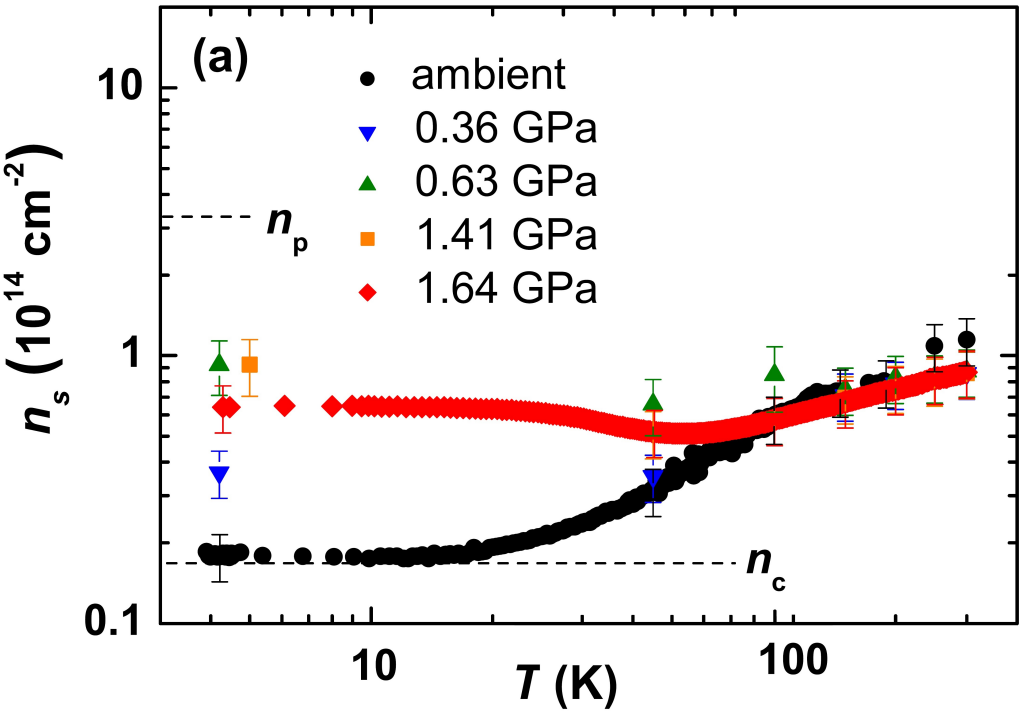

Figure 5.9: n_s versus T at ambient and different hydrostatic pressures. Error bars are shown exemplarily. Horizontal dashed lines indicate the expected sheet carrier density $n_p \approx 3.3 \times 10^{14}$ cm^{-2} if the charge of e/2 per surface unit-cell is transferred to the interface, and the critical sheet carrier density $n_c = 1.68 \times 10^{13}$ cm^{-2}, where a Lifshitz transition between d orbitals is expected (see text).

Despite the increase of the sheet resistance with increasing hydrostatic pressure at lower temperatures, the sheet carrier density(n_s) increases by a factor of three. Fig.5.9 shows that the sheet carrier concentration as a function of temperature measured under different hydrostatic pressure. In the intermediate temperature range $n_s(T)$ dips around 60 K. The increases of n_s may be explained by structural changes of STO or LAO under hydrostatic pressure. The bulk modulus for both LAO and STO is nearly the same for p $<$ 10 GPa [54, 55], which means that the pressure close to the interface should also be hydrostatic. For p $<$ 2 GPa, the STO does not exhibit any symmetry change [55]. Therefore, we do not expect any significant change in the energetic succession of t_{2g} sub-bands, which means t_{2g} are still the orbitals with the lowest energy and the first available to be occupied. Applying hydrostatic pressure on bulk STO shrinks its unit-cell volume by about 1%, primarily by equal bond-length reduction [56]. Therefore, the distance between atoms is reduced, increasing the crystal fields. Hence, the splitting between Ti 3d e_g and t_{2g} states increases and shifts the t_{2g} states downward in energy easily by a few meV [57], which may result in an enhanced thermal population by donor states. Biaxial compression of 1-2% in LAO/STO likewise leads to a significant increase of n_s [58]. In addition, structural changes in LAO have to be taken into account as well. The polar discontinuity at the

interface is accommodated through an intricate combination of ionic relaxation and electronic reconstruction which partially may compensate excess charge and thus lead to $n_s < n_p$ [59]. On the other hand, hydrostatic pressure may diminish the resulting buckling leading to an increase of n_s. For $T < 20$ K, our sheet carrier density is comparable with the sheet critical density n_c reported in [15], where a Lifshitz transition between d_{xy} and d_{xz}, d_{yz} is expected at $n_c = 1.7\text{x}10^{13}\text{cm}^{-2}$. As temperature increases, more carriers are activated and start to occupy d_{xz} and d_{yz} orbitals leading to a two-type-carrier transport for $n_s > n_c$. The one-type-carrier transport is expected only when $n_s < n_c$, where only d_{xy} orbitals are occupied. In Fig.5.10, we plot $ln(n_s)$ versus $1/T$ for temperatures > 50 K at ambient pressure. The red line represents the linear fitting for the data. The relation between charge carrier density and the activation energy can be expressed by $n_s(T) = e^{-\frac{E_A}{k_B T}}$, which leads to an activation energy of 5.8meV.

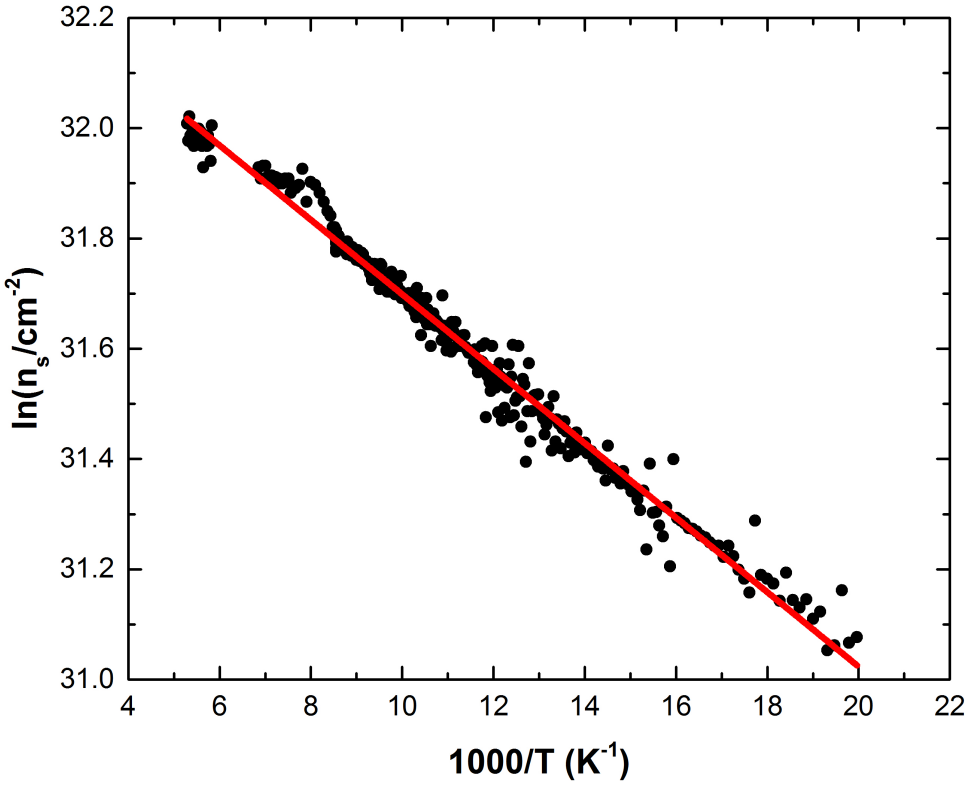

Figure 5.10: $\ln(n_s)$ versus $1/T$ for $T > 50$ K at ambient pressure. The graph shows an Arrhenius relation with activation energy of 5.8meV.

In contrast to the increase of the sheet carrier density with increasing pressure, measurements show that the Hall mobility decreases with increasing p and decreases with increasing T. The results of the measurements are shown in Fig.5.11.

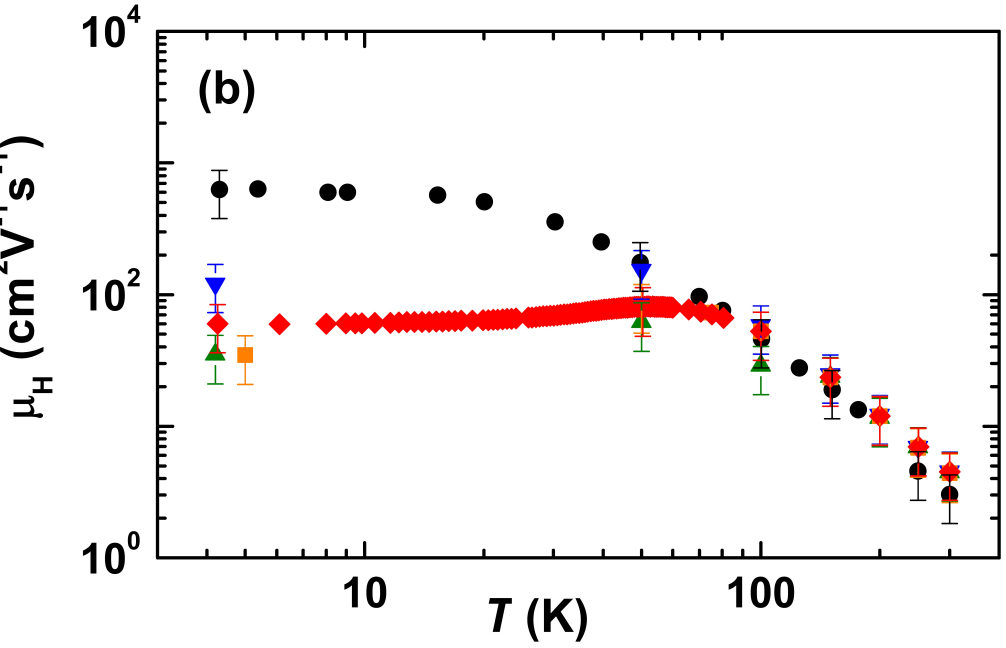

Figure 5.11: The Hall mobility(μ_H) as a function of T for LAO/STO sample grown at $p(O_2)$=10^{-5} mbar for different hydrostatic pressure. For $T > 110$ K the electron-phonon scattering is the dominant source of scattering.

The Hall mobility decreases with increasing the hydrostatic pressure at the low temperature range(T<60 K), from 700 cm^{2}V^{-1}s^{-1} at ambient pressure, to 60cm^{2}V^{-1}s^{-1} at p= 1.64 GPa and displays a T-independent behavior at a much lower level than observed at ambient pressure.

The sheet resistance relates to the Hall mobility(μ_H) and carrier concentration(n_s) as R_s $\propto$ (n_s μ_H) $^{-1}$. The increase in R_s below T_{min} suggests that μ_H has much more impact in determining the conductivity in the LAO/STO than n_s. As shown earlier, n_s actually increases with increasing p, however, it seems that this increase is completely dominated by the scattering of the carriers caused by the charged impurities. The strong decrease of μ_H with increasing p can be explained by the strong decrease of the static dielectric permittivity ε of STO. μ_H scales inversely with the scattering rate which, according to Fermi's golden rule for impurity scattering, is proportional to V^2 as discussed before. Hence in the low-temperature regime μ_H $\propto$ ε^2 is expected. Fig.5.12 shows μ_{Hn}=$\mu_H(p)/\mu_H(0)$ and ε_n^2=$[\varepsilon(p)/\varepsilon(0)]^2$ versus p at 4.2 K. Both curves show similar pressure dependence, which suggests direct impact of the dielectric permittivity on Hall mobility.

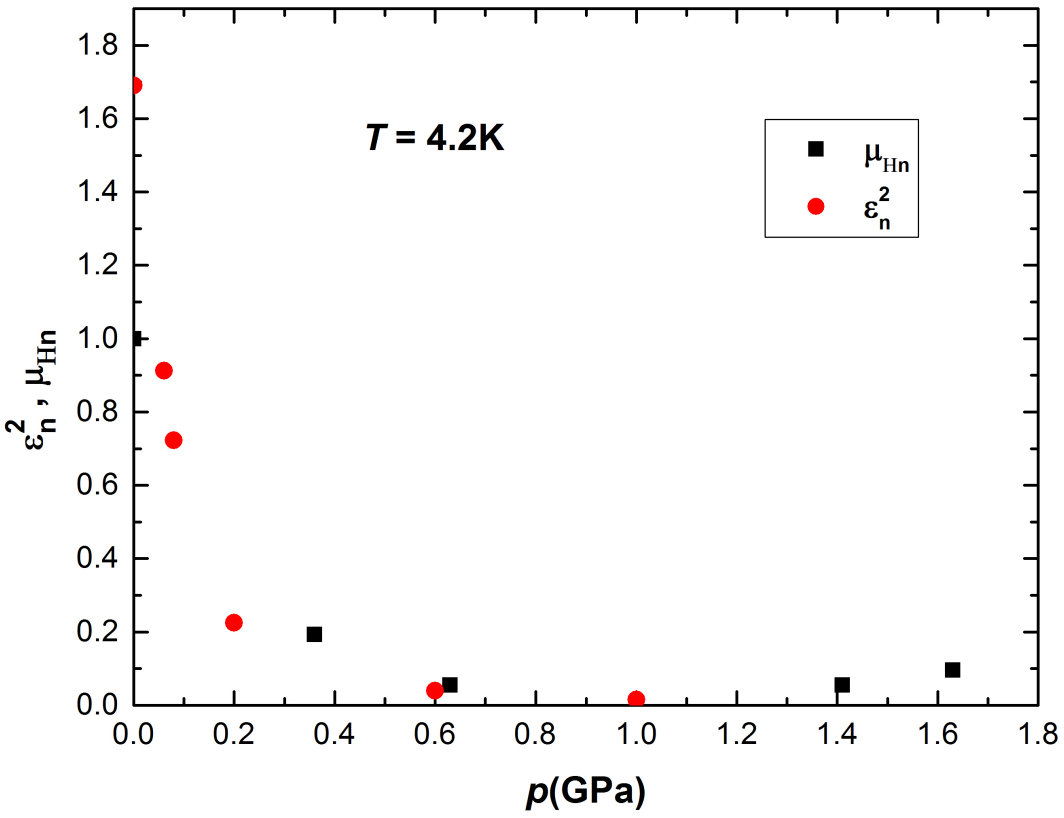

Figure 5.12: Normalized Hall mobility μ_{Hn}=μ_H(p)/μ_H(0) and normalized relative permittivity ε_n^2=[ε(p)/ε(0)]^2 as a function of hydrostatic pressure. The mobility points are taken at 4.2 K. The values of ε_n^2 are taken from Ref. [9]. The similarity in the behaviours of both curves suggests a correlation between the relative permittivity of STO and the Hall mobility of LAO/STO.

It is evident that both μ_{Hn} and ε_n^2 display nearly the same p-dependence, which explains the drop in the hall mobility of the sample as the hydrostatic pressure increases. At high T , ε_H is limited by polar (longitudinal phonon) scattering with a weaker dependence on ε, i.e., $\mu_H \propto \varepsilon$ [60]. In addition, ε of STO depends very weakly on p for $T > 200$ K. Hence, in this T range μ_H does not change appreciably with p, similarly to n_s, which already tends to saturate at ambient pressure for $T > 200$ K, see Fig.5.9. This explains the negligible p dependence of the transport properties for $T > 200$ K.

5.2 Magnetoresistance measurements on $LaAlO_3/SrTiO_3$.

Magnetoresistance (MR) measurements were performed on a LAO/STO heterostructure grown at $p(O_2) = 10^{-5}$mbar, MR(H)=[$R_s(H)$-$R_s(0)$]/$R_s(0)$ for LAO/STO under ambient and a pres-

sure of 1.64 GPa, at T = 4.2 K, 48 K and 150 K where R_s(H) is the sheet resistance as a function of magnetic field and $R_s(0)$ is the sheet resistance at $\mu_0 H$=0. MR versus $\mu_o H$ curves for LAO/STO are shown in Fig.5.13.

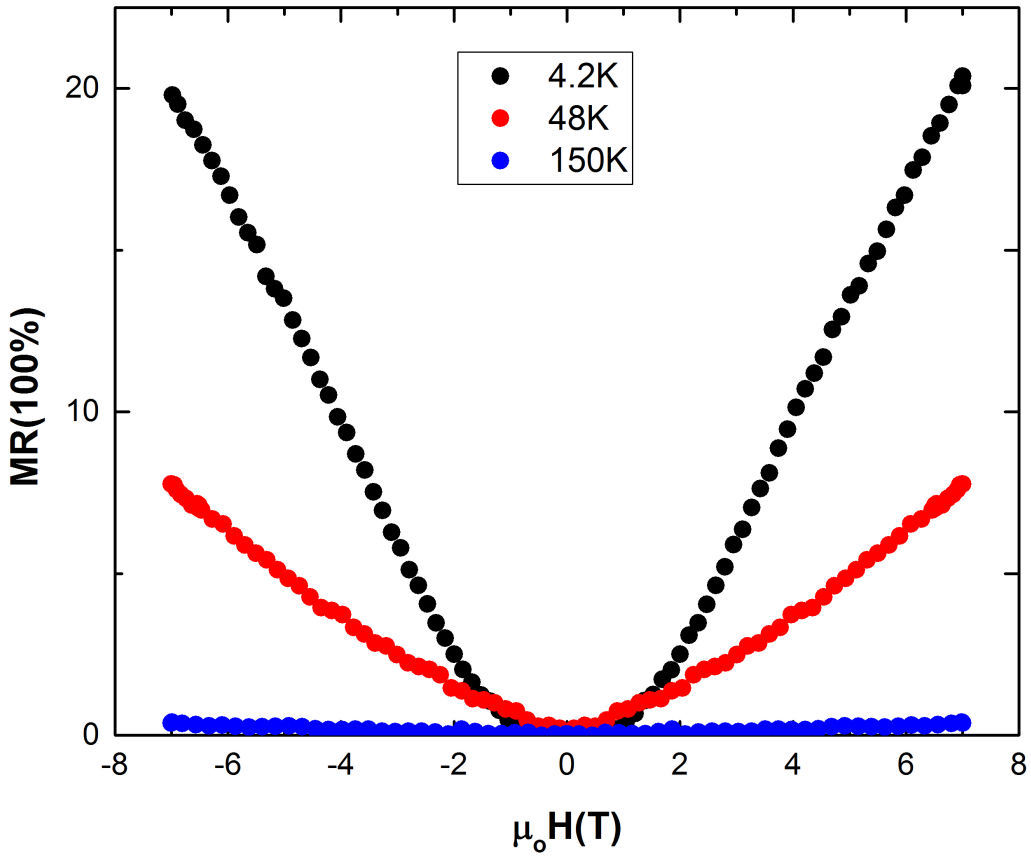

Figure 5.13: Magnetoresistance measurements versus $\mu_o H$ for the LAO/STO sample grown at $p(O_2)$= 10^{-5} mbar. The measurements are done under ambient pressure and at T = 4.2 K, 48 K and 150 K. MR is positive for the three temperatures. The maximum increase in the sheet resistance is observed at T = 4.2 K. MR decreases as T increases for the same field.

At ambient pressure, MR is always positive for the three temperatures and scales with $1/R_s(0)$ of the sample, i.e., MR strongly increases with decreasing R_s. The largest increase in the sheet resistance is observed at temperature of T =4.2 K, which is equal to 20% at $\mu_o H$ = 7T. The lowest MR is observed at T = 150 K, which is about 1%. The sheet resistance for the sample at T=4.2 K, 48 K and 150 K are 90Ω/□, 530Ω/□ and 2.73kΩ/□ respectively. The observed field dependence seems to be typical for LAO/STO [15]. The field dependence of MR at ambient pressure displays a quadratic dependence on H up to 4T at 4.2 K followed by

negative curvature. With increasing H and T MR displays contributions linear in H [61]. MR at low fields is obviously dominated by classical defect scattering following Kohler's rule.i.e. MR $\propto [H/R(0)]^2$. The increases in magnetic field increases the distance the electron travels due to the helical path of the electron moving in a magnetic field, leading to an increases in scattering rate, leading to an increase in R_s with increasing H.

MR under hydrostatic pressure of p=1.64 GPa was also measured for the same temperatures. The results are shown in Fig.5.14

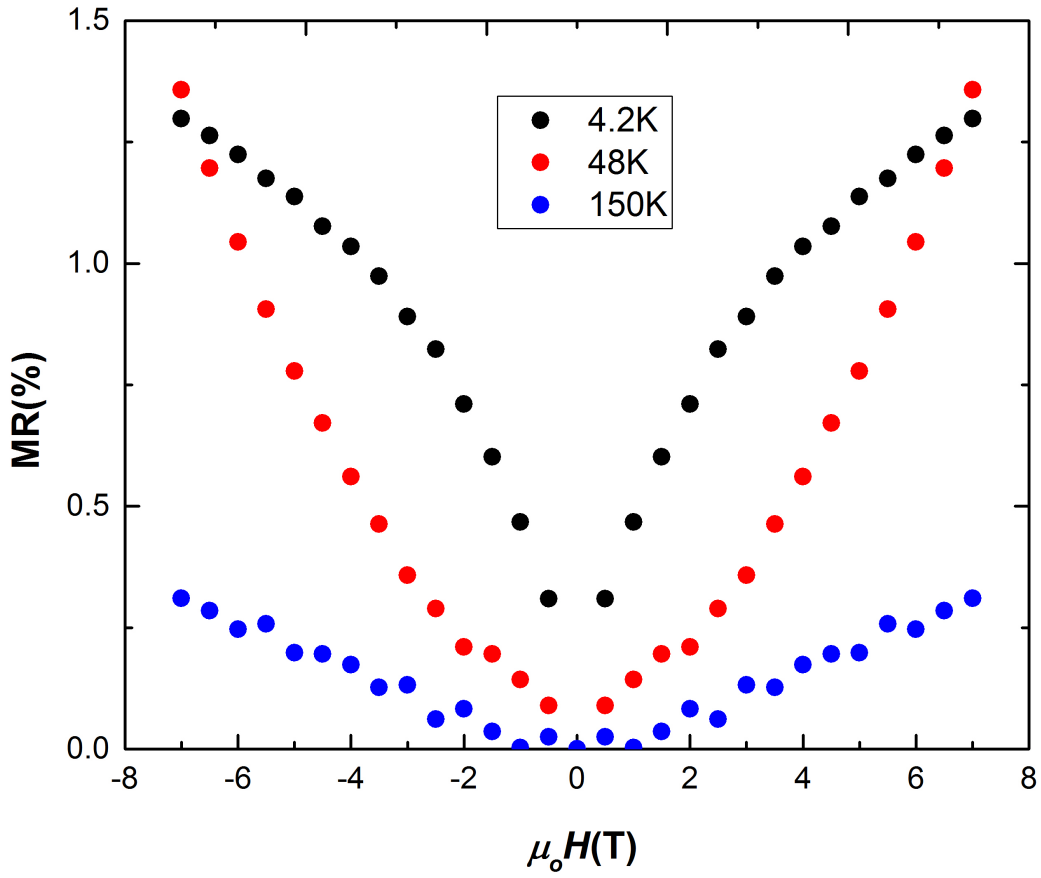

Figure 5.14: Magnetoresistance (MR) versus $\mu_o H$ for the LAO/STO heterostructures. The measurements were done at temperature of 4.2 K,48 K and 150 K under hydrostatic pressure of p=1.64 GPa.

At p=1.64 GPa, MR is also positive and is one order of magnitude less than ambient pressure (see Fig.5.14). The drop in MR is expected as R_s is increasing with increasing hydrostatic pressure. The MR at temperature of 150 K and 48 K show the effect of the classical scattering behaviour, as in the ambient pressure measurements. However, at T=4.2 K MR is reduced

strongly compared to the ambient pressure measurement at the same temperature possibly due to the large increase of the sheet resistance at T=4.2 K caused by the hydrostatic pressure as discussed earlier. The reduction of the classical scattering behaviour, enables the observation of other behaviours of MR. In this case, MR displays a steep increase already for small H and suggests a logarithmic increase at higher H.

5.3 Logarithmic correction to the conductance below 10 K.

To discuss the small increases of $R_s(T)$ below T=10 K in excess of R_{imp} we plot the negative conductance difference -$\Delta\sigma(T)$=-[1/$R_s(T)$-1/$R(T^*)$] versus ln(T/K) for T≤T*. The result is shown in Fig.5.15

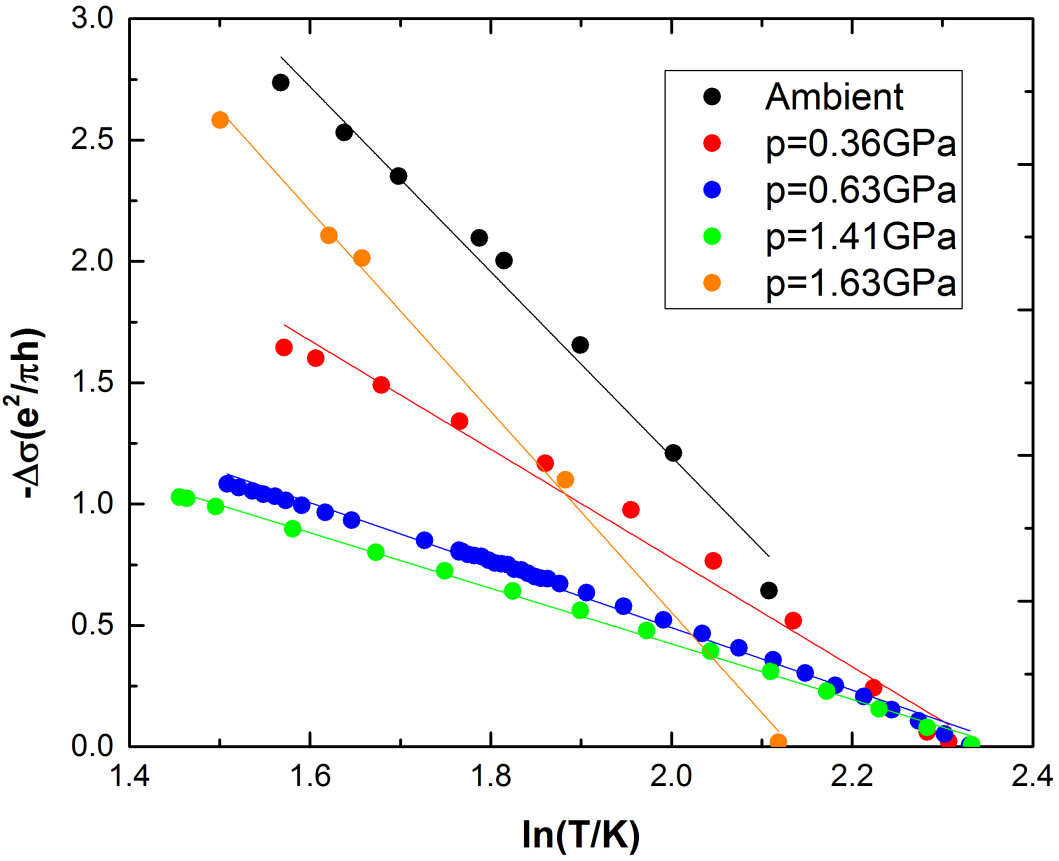

Figure 5.15: The negative conductance difference -$\Delta\sigma(T)$=-[1/$R_s(T)$-1/$R(T^*)$] versus ln(T/K) for LAO/STO sample at T ≤T*. The measurements were done under ambient and under different hydrostatic pressures.

-$\Delta\sigma(T)$ decreases linearly with increasing ln(T/K). The slope is of the order of $e^2/\pi h$, where h is the Planck constant, which indicates contributions from weak localization (WL) and/or electron-electron interaction(EEI) [62]. WL effects originate from the fact that in a disordered electronic systems, electrons move in a diffusive rather than ballistic nature. That is, electrons do not move in a straight line, but rather experience multiple scattering events by impurities in the sample, which results in a random path. R_s of the system is related to

the probability of the electrons to propagate between two given scattering points in the STO. In classical physics, this probability is simply the sum of the probabilities of a paths connecting the two points. However, in quantum mechanics, the total probability is the summation of the quantum-mechanical amplitudes of all paths rather than the probabilities themselves. Therefore, the correct formula for the probability for an electron to move from a point A to a point B includes the classical part (individual probabilities of diffusive paths) plus the number of interference terms. The interference terms are also present for the particular case A = B. Thus, these interference terms effectively increase the return probability where an electron will "wander around in a circle" than in the classical case, which leads to an increase in the net resistivity. In case of WL, the application of magnetic field leads to a decrease in R_s [59]. However, this was not observed in our MR measurements(see Figs.5.13 and 5.14). For two dimensional systems (2DES), both WL and EEI lead to a logarithmic dependence of $\Delta\sigma$ on T [63]:

$$\Delta\sigma(T)^{WL} = \alpha r e^2/2\pi^2\hbar \quad \ln(\frac{T}{T^o}) \tag{5.7}$$

and for the electron-electron interaction:

$$\Delta\sigma(T)^{EEI} = \lambda e^2/2\pi^2\hbar \quad \ln(\frac{T}{T^o}) \tag{5.8}$$

where αr and λ are dimensionless constants that depend on the material and display values close to unity.

In systems where Rashba spin-orbit interaction is present, which is the case for LAO/STO heterostructures, weak anti-localization (WAL) is expected more likely than weak localization(WL) [37], which leads to a positive correction to the conductance with decreasing T, resulting in:

$$\Delta\sigma(T)^{WAL} = -\alpha r e^2/2\pi^2\hbar \quad \ln(\frac{T}{T^o}) \tag{5.9}$$

Hence we expect a drop in R_s with decreasing T. However, this was not observed in $R_s(T)$ curves for any pressure, see Fig. 5.15.

In Fig. 5.16, the negative magnetoconductance $-\Delta\sigma(H) = 1/R_s(H)$-$1/R_s(0)$ is shown for p=1.64 GPa at T=4.2 K versus magnetic field μ_oH.

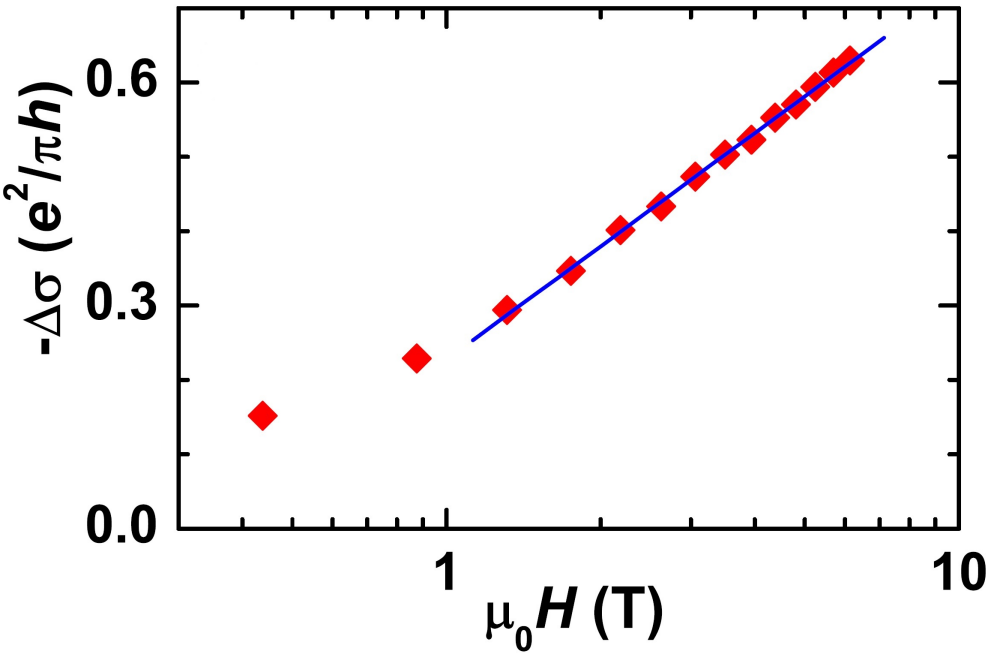

Figure 5.16: The negative magnetoconductance $-\Delta\sigma(H) = 1/R_s(H)$-$1/R_s(0)$ at p=1.64 GPa and T=4.2 K as a function of magnetic field $\mu_o H$. The negative magnetoconductance increases with increasing fields. -$\Delta\ \sigma$ displays a logarithmic field dependence for $\mu_o H > 1$T.

For EEI, a magnetic field dependence -$\Delta\sigma^{EEI}(H)$=$\lambda/2$ ($e^2/\pi h$)G(H) is expected. Where:

$$\begin{aligned} G(H) &= ln(h^*/1.3) \quad for \quad h^* > 1 \\ G(H) &= 0.084h^{*2} \quad for \quad h^* < 1 \end{aligned} \tag{5.10}$$

with $h^* = g\mu_B\mu_o H/k_B T$ [63] g, μ_B and k_B are the electron g factor, Bohr magneton and the Boltzmann constant, respectively.

At 4.2 K a magnetic field of 5 T corresponds to for $h^* \approx 1$. According to Eq. 5.10, we therefore expect a change in the behaviour from power law to logarithmic for $\mu_o H > 5$ T. This change in behaviour, however, is observed at $\mu_o H > 2$T instead of 5 T. One needs to keep in mind that in Ref. [64] spin orbit and spin scattering are not considered, which results in a

considerable increase in h*, and to -$\Delta\sigma^{EEI}$(H) $\propto$ ln(H)at smaller fields [61].

The observed change between 0 and 7 T of the conductance at 1.64 GPa is again of the order of $e^2/\pi h$. Similar changes in $\Delta\sigma(H)$ and $\Delta\sigma(T)$ are obviously caused by comparable changes in T and H, i.e., g$\mu_B\mu_o\Delta$H $\approx k_B\Delta\, T$. Hence, the corrections to the conductance below T^* with respect to their T and H dependencies are consistently described by EEI. However, the positive MR(H) of LAO/STO is often alternatively discussed in the context of WAL [64, 37] .

For weak localization, the magnetoconductance of a 2D layer is given by [65]:

$$\Delta\sigma(H_{si}, H_{tr}, H) = \frac{e^2}{h}\left(\frac{3}{2}f(H/H_{tr}) - \frac{1}{2}f(H/H_{si})\right) \tag{5.11}$$

where

$$f(b) = \frac{1}{\pi}\left(\psi(\frac{1}{2} + \frac{1}{b}) - ln(b)\right) \tag{5.12}$$

The triplet and singlet states contributions are described by:

$$H_{tr} = 4H_{SO} + H_{\phi} \tag{5.13}$$

$$H_{si} = H_{\phi} \tag{5.14}$$

where ψ is the di-gamma function, H_ϕ is the inelastic field, describing the phase relaxation process by inelastic scattering and the H_{SO} is the spin orbit-field, describing spin relaxation by spin-orbit interaction. If spin-orbit interaction in LAO/STO was absent,this would lead to a positive $\Delta\sigma(H_\phi,H) = (e^2/2h)f(H/H_\phi)$, whereas in case of strong spin-orbit coupling, $\Delta\sigma(H_\phi,H)$ = -$(e^2/2h)f(H/H_{phi})$ becomes negative. The phase coherence length is given by L_ϕ = $[h/(8\pi eH_\phi)]^{1/2}$

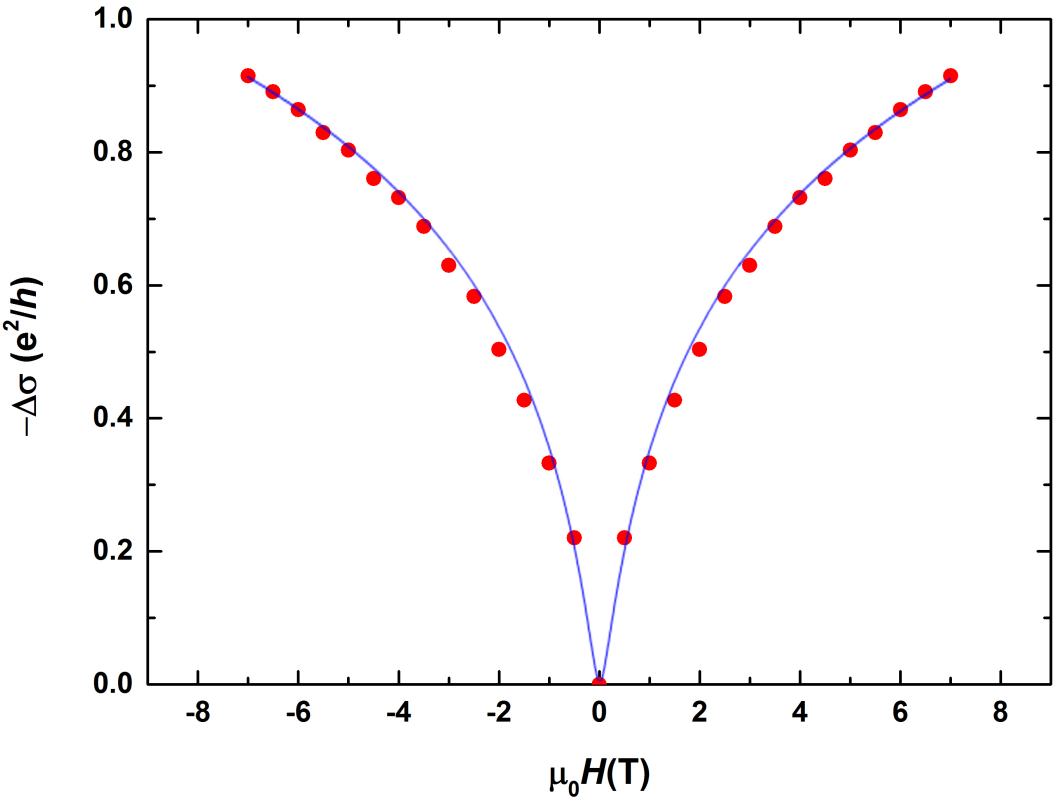

Figure 5.17: The negative magnetoconductance $-\Delta\sigma$ versus $\mu_o H$ at p=1.64 GPa and T=4.2 K. The solid line indicates a fit to Eq. 5.11

In order to check whether our data are compatible with WAL, we plot (Fig. 5.17) the negative magnetoconductance $-\Delta\sigma(H) = 1/R_s(H)\text{-}1/R_s(0)$ versus $\mu_o H$ at p=1.64 GPa and T=4.2 K. The fit of $\text{-}\Delta\sigma(H)$ according to Eq. 5.11 is shown by the solid line. The data can be well described in terms of 2D WAL [62, 65, 64] if the conductance is multiplied by a factor 2.2. The inelastic field $H_\Phi = 75$ mT and a spin-orbit field $H_{SO} > 8$T, deduced from the fit compares well to data reported in Ref. [37] . However, in view of our observations described above, EEI seems to be more likely responsible for the observed magnetoconductance at low T.

Chapter 6

Summary

We have successfully prepared high quality $LaAlO_3/SrTiO_3$ heterostructures using pulsed laser deposition technique under optimized parameters. The structural and electrical properties of these heterostructures were investigated by means of atomic force microscope, X-ray, high resolution (aberration corrected) transition electron microscope (HR(AC)TEM). New hardware, including a pressure cell, were designed and built to allow for measurement of the electrical resistivity and magnetoresistance under hydrostatic pressure. The sheet resistance was measured as a function of temperature between 4.2 K and 300 K at ambient and at different hydrostatic pressure up to p=1.46 GPa. Magnetoresistance measurements were performed up to 7T on the same samples at different temperature and pressure.

Our study documents the very vital role of donor states and the relative permittivity(ε_r) of STO(especially at low T) for the transport properties of the 2DES in LAO/STO heterostructures under hydrostatic pressure. For T >100 K, the transport properties are determined by electron-phonon scattering resulting in $R_s \propto T^2$. R_s depends only very little on p, due to the small dependence of ε_r on hydrostatic pressure at this temperature range. However, for 10 K < T < 100 K, ε_r is highly dependant on both p and T, strongly affecting R_s(T) by impurity scattering due to, most likely, to oxygen vacancies. Thermal activation of trapped charge carriers and the para-electric behavior of STO lead to a distinct T dependence of the impurity scattering in this temperature range with a minimum in $R_s(T)$ occurring at T_{min}, separating the metallic ($T > T_{min}$) and nonmetallic ($T < T_{min}$) regimes of the 2DES. The strong p dependence of the dielectric permittivity ε(p) of STO primarily is responsible for the incipient localization of charge carriers, i.e., the strong decrease of μ_H and increase of R_s with increasing p. Hence, it is the p and T dependencies of $N_i(T)$ and $\varepsilon(p,T)$, rather than the Kondo effect, that entail the $R_s(T)$ minimum under pressure. The small negative logarithmic corrections to the conductance

observed for 4.2 K $< T <$ 10 K are attributed to electron-electron interactions.

Our work not only increased our understanding of theses systems, but also it opened the door to new interesting experiments. One of which is the application of gate voltage on the sample while under the maximum hydrostatic pressure. The application of the electric field on the sample improves the conductivity by increasing the number of charge carriers in the system. The drop in ε due to the application of hydrostatic pressure, leads to reduction in the screening of the applied electric field, which helps achieve higher electric field on the carrier using lower voltages than the ones used at ambient pressure. This experiment might help understand the contribution of the charge carrier concentration and the Hall mobility on the sheet resistance, and see if the increase in the sheet carrier concentration can reverse the drop in the Hall mobility caused by the hydrostatic pressure at low temperature.

Acknowledgments

I would like to express my gratitude and appreciation to Dr. Dirk Fuchs at the Institute for Solid State Physics in the KIT-CN for the guidance and knowledge he provided me during my years as a PhD student in the institute. His supervision over my work had a profound impact on the quality and value the of my thesis.

I also would like to thank my colleagues in the institute, Dr. Schneider, Dr. Zaitsev and Andry Beck for their valuable help and advice which helped me in compacting many of my problems through the years.

Bibliography

[1] M. Koster, G. Huijben and G. Rijnders. Epitaxial Growth of Complex Metal Oxides . *Woodhead Publishing*, 2015.

[2] H. M. Manasevit and I. S. Gergis and A. B. Jones. Electron mobility enhancement in epitaxial multilayer Si-$Si_{1-x}Ge_x$ alloy films on (100) Si. *Applied Physics Letters*, 41:464, 1982.

[3] J. Zabaleta, V. S. Borisov, R. Wanke, H. O. Jeschke, S. C. Parks, B. Baum, A. Teker, T. Harada, K. Syassen, T. Kopp, N. Pavlenko, R. Valentí, and J. Mannhart. Hydrostatic pressure response of an oxide-based two-dimensional electron system. *Phys. Rev. B*, 93:235117, 2016.

[4] D. Fuchs, E. Arac, C. Pinta, S. Schuppler, R. Schneider, and H. v. Löhneysen. Tuning the magnetic properties of $LaCoO_3$ thin films by epitaxial strain. *Phys. Rev. B*, 77:014434, 2008.

[5] J. H. Haeni, P. Irvin, W. Chang, R. Uecker, P. Reiche, Y. L. Li, S. Choudhury, W. ian, M. E. Hawley, B. Craigo, A. K. Tagantsev, X. Q. Pan, S. K. Streiffer, L. Q. Chen, S. W. Kirchoefer, J. Levy, and D. G. Schlom. Room-temperature ferroelectricity in strained $SrTiO_3$. *Nature*, 430:758, 2004.

[6] A. P. Drozdov, M. I. Eremets, . A. Troyan, V. Ksenofontov, and S. I. Shylin. Conventional superconductivity at 203 Kelvin at high pressures in the sulfur hydride system. *Nature*, 525:73, 2015.

[7] L. Gao, Y. Y. Xue, F. Chen, Q. Xiong, R. L. Meng, D. Ramirez, C. W. Chu, J. H. Eggert, and H. K. Mao. Superconductivity up to 164 K in $HgBa_2Ca_{m-1}Cu_mO_{2m+2+\delta}$(m=1, 2, and 3) under quasihydrostatic pressures. *Phys. Rev. B*, 50:4260, 1994.

[8] F. Le Marrec, A. Demuer, D. Jaccard, J.M. Triscone, M. K. Lee, and C. B. Eom. Magnetic behavior of epitaxial $SrRuO_3$ thin films under pressure up to 23 GPa. *Applied Physics Letters*, 80:2338, 2002.

[9] Ruiping Wang, Norihiko Sakamoto, and Mitsuru Itoh. Effects of pressure on the dielectric properties of $SrTi^{18}O_3$ and $SrTi^{16}O_3$ single crystals. *Phys. Rev. B*, 62:R3577, 2000.

[10] R. A. van der Berg, P. W. M.Blom, J. F. M. Cillessen, and R. M. Wolf. Field dependent permittivity in metal-semiconducting $SrTiO_3$ Schottky diodes. *Applied Physics Letters*, 66:697, 1995.

[11] Zhicheng Zhong, Anna Tóth, and Karsten Held. Theory of spin-orbit coupling at $LaAlO_3/SrTiO_3$ interfaces and $SrTiO_3$ surfaces. *Phys. Rev. B*, 87:161102, 2013.

[12] S. McKeown Walker, S. Ricco, F. Y. Bruno, A. de la Torre, A. Tamai, E. Golias, A. Varykhalov, D. Marchenko, M. Hoesch, M. S. Bahramy, P. D. C. King, J. Sanchez-Barriga, and F. Baumberger. Absence of giant spin splitting in the two-dimensional electron liquid at the surface of $SrTiO_3$ (001). *Phys. Rev. B*, 93:245143, 2016.

[13] A. F. Santander-Syro, O. Copie, T. Kondo, F. Fortuna, S. Pailhes, R. Weht, X. G. Qiu, F. Bertran, A. Nicolaou, A. Taleb-Ibrahimi, P. Le Fevre, G. Herranz, M. Bibes, N. Reyren, Y. Apertet, P. Lecoeur, A. Barthelemy, and M. J. Rozenberg. Two-dimensional electron gas with universal subbands at the surface of $SrTiO_3$. *Nature*, 469:189, 2011.

[14] A. D. Caviglia, S. Gariglio, N. Reyren, D. Jaccard, T. Schneider, M. Gabay, S. Thiel, G. Hammerl, J. Mannhart, and J.-M. Triscone. Electric field control of the $LaAlO_3/SrTiO_3$ interface ground state. *Nature*, 456:624, 2008.

[15] A. Joshua, S. Pecker, J. Ruhman, E. Altman, and S. Ilani. A universal critical density underlying the physics of electrons at the $LaAlO_3/SrTiO_3$ interface. *Nature Communications*, 3:1129, 2012. Article.

[16] K. v. Klitzing, G. Dorda, and M. Pepper. New method for high-accuracy determination of the fine-structure constant based on quantized hall resistance. *Phys. Rev. Lett.*, 45:494, 1980.

[17] P. Grünberg, R. Schreiber, Y. Pang, M. B. Brodsky, and H. Sowers. Layered Magnetic Structures: Evidence for Antiferromagnetic Coupling of Fe Layers across Cr Interlayers. *Phys. Rev. Lett.*, 57:2442, 1986.

[18] A. Ohtomo and H. Y. HwangM. A high-mobility electron gas at the $LaAlO_3/SrTiO_3$ heterointerface. *Nature*, 427:423, 2004.

[19] M. Salluzzo, J. C. Cezar, N. B. Brookes, V. Bisogni, G. M. De Luca, C. Richter, S. Thiel, J. Mannhart, M. Huijben, A. Brinkman, G. Rijnders, and G. Ghiringhelli. Orbital reconstruction and the two-dimensional electron gas at the $LaAlO_3/SrTiO_3$ Interface. *Phys. Rev. Lett.*, 102:166804, 2009.

[20] E. Breckenfeld, N. Bronn, J. Karthik, A. R. Damodaran, S. Lee, N. Mason, and L. W. Martin. Effect of growth induced nonstoichiometry on interfacial conductance in $LaAlO_3/SrTiO_3$. *Phys. Rev. Lett.*, 110:196804, 2013.

[21] Mark Huijben, Guus Rijnders, Dave H. A. Blank, Sara Bals, Sandra Van Aert, Jo Verbeeck, Gustaaf Van Tendeloo, Alexander Brinkman, and Hans Hilgenkamp. Electronically coupled complementary interfaces between perovskite band insulators. *Nat Mater*, 5:556, 2006.

[22] G. Herranz, M. Basletić, M. Bibes, C. Carrétéro, E. Tafra, E. Jacquet, K. Bouzehouane, C. Deranlot, A. Hamzić, J.-M. Broto, A. Barthélémy, and A. Fert. High Mobility in $LaAlO_3/SrTiO_3$ Heterostructures: Origin, Dimensionality, and Perspectives. *Phys. Rev. Lett.*, 98:216803, 2007.

[23] Alexey Kalabukhov, Robert Gunnarsson, Johan Borjesson, Eva Olsson, Tord Claeson, and Dag Winkler. Effect of oxygen vacancies in the $SrTiO_3$ substrate on the electrical properties of the $LaAlO_3/SrTiO_3$ interface. *Phys. Rev. B*, 75:121404, 2007.

[24] L Qiao, T C Droubay, V Shutthanandan, Z Zhu, P V Sushko, and S A Chambers. Thermodynamic instability at the stoichiometric $LaAlO_3/SrTiO_3$ (001) interface. *Journal of Physics: Condensed Matter*, 22:312201, 2010.

[25] N. Reyren, S. Thiel, A. D. Caviglia, L. Fitting Kourkoutis, G. Hammerl, C. Richter, C. W. Schneider, T. Kopp, A.-S. R. etschi, D. Jaccard, M. Gabay, D. A. Muller, J.-M. Triscone, and J. Mannhart. Superconducting Interfaces Between Insulating Oxides. *Science*, 317:1196, 2007.

[26] Seung-Gu Lim, Stas Kriventsov, Thomas N. Jackson, J. H. Haeni, D. G. Schlom, A. M. Balbashov, R. Uecker, P. Reiche, J. L. Freeouf, and G. Lucovsky. Dielectric functions and optical bandgaps of high-k dielectrics for metal-oxide-semiconductor field-effect transistors by far ultraviolet spectroscopic ellipsometry. *Journal of Applied Physics*, 91:4500, 2002.

[27] Manuel Cardona. Optical properties and band structure of $SrTiO_3$ and $BaTiO_3$. *Phys. Rev.*, 140:651, 1965.

[28] J.G. Bednorz and H.J. Scheel. Flame-fusion growth of $SrTiO_3$. *Journal of Crystal Growth*, 41:5, 1977.

[29] S. Geller and V. B. Bala. Crystallographic studies of perovskite-like compounds. II. Rare earth alluminates. *Acta Crystallographica*, 9:1019, 1956.

[30] Masashi Kawasaki, Kazuhiro Takahashi, Tatsuro Maeda, Ryuta Tsuchiya, Makoto Shinohara, Osamu Ishiyama, Takuzo Yonezawa, Mamoru Yoshimoto, and Hideomi Koinuma. Atomic Control of the $SrTiO_3$ Crystal Surface. *Science*, 266:1540, 1994.

[31] Gertjan Koster, Boike L. Kropman, Guus J. H. M. Rijnders, Dave H. A. Blank, and Horst Rogalla. Quasi-ideal strontium titanate crystal surfaces through formation of strontium hydroxide. *Applied Physics Letters*, 73:2920, 1998.

[32] W. A. Harrison, E. A. Kraut, J. R. Waldrop, and R. W. Grant. Polar heterojunction interfaces. *Phys. Rev. B*, 18:4402, 1978.

[33] G. Herranz, F. SÃ¡nchez, N. Dix, M. Scigaj, and J. Fontcuberta. High mobility conduction at (110) and (111) $LaAlO_3/SrTiO_3$ interfaces. *Scientific Reports*, 2:758, 2012.

[34] P. R. Willmott, S. A. Pauli, R. Herger, C. M. Schlepütz, D. Martoccia, B. D. Patterson, B. Delley, R. Clarke, D. Kumah, C. Cionca, and Y. Yacoby. Structural Basis for the Conducting Interface between $LaAlO_3$ and $SrTiO_3$. *Phys. Rev. Lett.*, 99:155502, 2007.

[35] Zhicheng Zhong, Philipp Wissgott, Karsten Held, and Giorgio Sangiovanni. Microscopic understanding of the orbital splitting and its tuning at oxide interfaces. *EPL (Europhysics Letters)*, 99:37011, 2012.

[36] M. Basletic, J.-L. Maurice, C. Carretero, G. Herranz, O. Copie, M. Bibes, E. Jacquet, K. Bouzehouane, S. Fusil, and A. Barthelemy. Mapping the spatial distribution of charge carriers in $LaAlO_3/SrTiO_3$ heterostructures. *Nat Mater*, 7:621, 2008.

[37] A. D. Caviglia, M. Gabay, S. Gariglio, N. Reyren, C. Cancellieri, and J.-M. Triscone. Tunable Rashba Spin-Orbit Interaction at Oxide Interfaces. *Phys. Rev. Lett.*, 104:126803, 2010.

[38] R. Bachelet, F. SÃ¡nchez, F. J. Palomares, C. Ocal, and J. Fontcuberta. Atomically flat SrO-terminated $SrTiO_3(001)$ substrate. *Applied Physics Letters*, 95, 2009.

[39] A. Biswas, P. B. Rossen, C.-H. Yang, W. Siemons, M.-H. Jung, I. K. Yang, R. Ramesh, and Y. H. Jeong. Universal Ti-rich termination of atomically flat $SrTiO_3$ (001), (110), and (111) surfaces. *Applied Physics Letters*, 98:051904, 2011.

[40] D. Dijkkamp, T. Venkatesan, X. D. Wu, S. A. Shaheen, N. Jisrawi, Y. H. Min-Lee, W. L. McLean, and M. Croft. Preparation of YBaCu oxide superconductor thin films using pulsed laser evaporation from high T_c bulk material. *Applied Physics Letters*, 51:619, 1987.

[41] Y. Z. Chen, N. Bovet, F. Trier, D. V. Christensen, F. M. Qu, N. H. Andersen, T. Kasama, W. Zhang, R. Giraud, J. Dufouleur, T. S. Jespersen, J. R. Sun, A. Smith, J. NygArd, L. Lu, B. B chner, B. G. Shen, S. Linderoth, and N. Pryds. A high-mobility two-dimensional electron gas at the spinel/perovskite interface of γ-$Al_2O_3/SrTiO_3$. *Nature Communications*, 4:1371, 2013.

[42] S. Thiel, G. Hammerl, A. Schmehl, C. W. Schneider, and J. Mannhart. Tunable quasi-two-dimensional electron gases in oxide heterostructures. *Science*, 313:1942, 2006.

[43] Keiichi Yokogawa, Keizo Murata, Harukazu Yoshino, and Shoji Aoyama. Solidification of high-pressure medium daphne 7373. *Japanese Journal of Applied Physics*, 46:3636, 2007.

[44] A Eiling and J S Schilling. Pressure and temperature dependence of electrical resistivity of Pb and Sn from 1-300K and 0-10 GPa-use as continuous resistive pressure monitor accurate over wide temperature range; superconductivity under pressure in Pb, Sn and In. *Journal of Physics F: Metal Physics*, 11:623, 1981.

[45] L. J. Van der Pauw. A method of measuring the resistivity and hall coefficient on lamellae of arbitrary shape. *Philips Technical Review*, 20.

[46] A. Brinkman, M. Huijben, M. van Zalk, J. Huijben, U. Zeitler, J. C. Maan, W. G. van der Wiel, G. Rijnders, D. H. A. Blank, and H. Hilgenkamp. Magnetic effects at the interface between non-magnetic oxides. *Nat Mater 6, 493*, 2007.

[47] D. van der Marel, J. L. M. van Mechelen, and I. I. Mazin. Common Fermi-liquid origin of T^2 resistivity and superconductivity in n-type $SrTiO_3$. *Phys. Rev. B*, 84:205111, 2011.

[48] Snir Seri, Moty Schultz, and Lior Klein. Thermally activated recovery of electrical conductivity in $LaAlO_3/SrTiO_3$. *Phys. Rev. B*, 87:125110, 2013.

[49] Z. Q. Liu, D. P. Leusink, X. Wang, W. M. Lü, K. Gopinadhan, A. Annadi, Y. L. Zhao, X. H. Huang, S. W. Zeng, Z. Huang, A. Srivastava, S. Dhar, T. Venkatesan, and Ariando.

Metal-insulator transition in $SrTiO_{3-x}$ thin films induced by frozen-out carriers. *Phys. Rev. Lett.*, 107:146802, 2011.

[50] S. Thiel, C. W. Schneider, L. Fitting Kourkoutis, D. A. Muller, N. Reyren, A. D. Caviglia, S. Gariglio, J.-M. Triscone, and J. Mannhart. Electron scattering at dislocations in $LaAlO_3/SrTiO_3$ interfaces. *Phys. Rev. Lett.*, 102:046809, 2009.

[51] Lytle Farrel W. X-ray diffractometry of low temperature phase transformations in strontium titanate. *Journal of Applied Physics*, 35:2212, 1964.

[52] Z. Q. Liu, C. J. Li, W. M. Lu, X. H. Huang, Z. Huang, S. W. Zeng, X. P. Qiu, L. S. Huang, A. Annadi, J. S. Chen, J. M. D. Coey, T. Venkatesan, and Ariando. Origin of the Two-Dimensional Electron Gas at $LaAlO_3/SrTiO_3$ Interfaces: The Role of Oxygen Vacancies and Electronic Reconstruction. *Phys. Rev. X*, 3:021010, 2013.

[53] John H. Barrett. Dielectric constant in perovskite type crystals. *Phys. Rev.*, 86:118, 1952.

[54] A Hachemi, H Hachemi, A Ferhat-Hamida, and L Louail. Elasticity of $SrTiO_3$ perovskite under high pressure in cubic, tetragonal and orthorhombic phases. *Physica Scripta*, 82:025602, 2010.

[55] M. Guennou, P. Bouvier, G. Garbarino, and J. Kreisel. Structural investigation of $LaAlO_3$ up to 63 GPa. *J. Phys.: Condens. Matter 23, 395401*, 2011.

[56] Mael Guennou, Pierre Bouvier, Jens Kreisel, and Denis Machon. Pressure-temperature phase diagram of $SrTiO_3$ up to 53 GPa. *Phys. Rev. B*, 81:054115, 2010.

[57] V. Izyumov V. Anisimov. *Electronic Structure of Strongly Correlated Materials*. Springer, 2010.

[58] Z. Huang, Z. Q. Liu, M. Yang, S. W. Zeng, A. Annadi, W. M. Lü, X. L. Tan, P. F. Chen, L. Sun, X. Renshaw Wang, Y. L. Zhao, C. J. Li, J. Zhou, K. Han, W. B. Wu, Y. P. Feng, J. M. D. Coey, T. Venkatesan, and Ariando. Biaxial strain-induced transport property changes in atomically tailored $SrTiO_3$-based systems. *Phys. Rev. B*, 90:125156, 2014.

[59] Rossitza Pentcheva and Warren E. Pickett. Ionic relaxation contribution to the electronic reconstruction at the n-type $LaAlO_3/SrTiO_3$ interface. *Phys. Rev. B*, 78:205106, 2008.

[60] J. H. Davis. *The Physics of Low-Dimensional Semiconductors*. Cambridge University Press, Cambridge, 1998.

[61] A. .P Pippard. *Magnetoresistance in Metals*. Cambridge university press, Cambridge, 1993.

[62] Patrick A. Lee and T. V. Ramakrishnan. Disordered electronic systems. *Rev. Mod. Phys.*, 57:287, 1985.

[63] D. J. Bishop, R. C. Dynes, and D. C. Tsui. Magnetoresistance in Si metal-oxide-semiconductor field-effect transitors: Evidence of weak localization and correlation. *Phys. Rev. B*, 26:773, 1982.

[64] Gerd Bergmann. Weak localization in thin films. *Physics Reports*, 107:1, 1984.

[65] Shinobu Hikami, Anatoly I. Larkin, and Yosuke Nagaoka. Spin-orbit interaction and magnetoresistance in the two dimensional random system. *Progress of Theoretical Physics*, 63:707, 1980.